Atmospheric Research 183 (2017) 151–165

Contents lists available at ScienceDirect

Atmospheric Research

journal homepage: www.elsevier.com/locate/atmosres

Diversity on subtropical and polar cirrus clouds properties as derived from both ground-based lidars and CALIPSO/CALIOP measurements

Carmen Córdoba-Jabonero [a,*], Fabio J. S. Lopes [b,c], Eduardo Landulfo [c], Emilio Cuevas [d], Héctor Ochoa [e], Manuel Gil-Ojeda [a]

[a] Instituto Nacional de Técnica Aeroespacial (INTA), Atmospheric Research and Instrumentation Branch, Ctra. Ajalvir km. 4, Torrejón de Ardoz, 28850, Madrid, Spain
[b] Instituto de Astronomia, Geofisica e Ciências Atmosféricas (IAG), Universidade de São Paulo (USP), São Paulo, Brazil
[c] Instituto de Pesquisas Energéticas e Nucleares (IPEN), Center for Lasers and Applications, São Paulo, Brazil
[d] Agencia Estatal de Meteorología (AEMET), Atmospheric Research Centre of Izaña, Sta. Cruz de Tenerife, Spain
[e] Instituto Antártico Argentino/Dirección Nacional del Antártico (IAA/DNA), Buenos Aires, Argentina

ARTICLE INFO

Article history:
Received 14 December 2015
Received in revised form 9 August 2016
Accepted 17 August 2016
Available online 20 August 2016

Keywords:
CALIPSO/CALIOP
Cirrus Cloud Optical Depth (CCOD)
Cirrus clouds
Lidar
Polar regions
Subtropical latitudes

ABSTRACT

Cirrus (Ci) cloud properties can change significantly from place to place over the globe as a result of weather processes, reflecting their likely different radiative and climate implications. In this work Cirrus clouds (Ci) features observed in late autumn/early winter season at both subtropical and polar latitudes are examined and compared to CALIPSO/CALIOP observations. Lidar measurements were carried out in three stations: São Paulo (MSP, Brazil) and Tenerife (SCO, Canary Islands, Spain), as subtropical sites, and the polar Belgrano II base (BEL, Argentina) in the Antarctic continent. The backscattering ratio (BSR) profiles and the top and base heights of the Ci layers together to their Cirrus Cloud Optical Depth (CCOD) and Lidar Ratio (LR) for Ci clouds were derived. In addition, temperatures at the top and base boundaries of the Ci clouds were also obtained from local radiosoundings to verify pure ice Ci clouds occurrence using a given temperature top threshold (<−38 °C). Ci clouds observed along the day were assembled in groups based on their predominant CCOD, and classified according to four CCOD-based categories. Ci clouds were found to be vertically-distributed in relation with the temperature, forming subvisual Ci clouds at lower temperatures and higher altitudes than other Ci categories at both latitudes. Discrepancies shown on LR values for the three stations, but mainly remarked between subtropical and polar cases, can be associated to different temperature regimes for Ci formation, influencing the internal ice habits of the Ci clouds, and hence likely affecting the LR derived for the Ci layer. In comparison with literature values, daily mean CCOD/LR for SCO (0.4 ± 0.4/21 ± 10 sr), MSP (0.5 ± 0.5/27 ± 5 sr) and BEL (0.2 ± 0.3/28 ± 9 sr) are in good agreement; however, the variability of the Ci optical features along the day present large discrepancies. In comparison with CALIOP data, Ci clouds are observed at similar altitudes (around 10–13 km height); however, differences are found mostly in CCOD values for subtropical Ci clouds, whereas LR values are in a closer agreement. These differences are carefully examined in relation with the closest CALIPSO overpass time and distance from the station (>70 km far), inferring the irregular extension and inhomogeneity of the Ci clouds over each study area. These considerations can be useful for assimilation of the Ci features into climate models and evaluation of future space-borne lidar observations of Ci clouds, especially for the future ESA/Copernicus-Sentinel and ESA/EarthCARE missions.

1. Introduction

Both weather and climate are evidently affected by Cirrus (Ci) clouds. Indeed, their role in the radiation balance of the Earth-atmosphere system can be regionally and globally observed (Liou, 1986; Stephens, 2005; Yorks et al., 2009; Yang et al., 2012) as cooling or heating modulations. What it still a puzzle is the response of Ci clouds to factors related to anthropogenic climate changes, i.e. greenhouse effect (Iacono et al., 2008), or increasing upper tropospheric contamination from enhanced aviation circulation (Boucher, 1999). The Ci cloud radiation transfer properties could alter, either enhancing or negating, the supposed global warming effect linked to aerosols as reported in the last Intergovernmental Panel on Climate Change (IPCC, 2013) (Boucher et al., 2013). In particular, Cirrus aircraft-induced contrails could increase the albedo of the upper troposphere, modifying the warming effect associated to greenhouse gases (Burkhardt and

* Corresponding author.
E-mail address: cordobajc@inta.es (C. Córdoba-Jabonero).
URL: http://www.inta.es/atmosfera (C. Córdoba-Jabonero).

http://dx.doi.org/10.1016/j.atmosres.2016.08.015
0169-8095/

Kärcher, 2011). The balance between the infrared greenhouse warming and solar albedo cooling depends on both Ci cloud altitude and their microphysical features (Myhre et al., 2013).

In this context cloud height plays a significant role. Tropical Cirrus located at high altitudes can act as effective greenhouse modulators. In opposition, low-altitude Cirrus over Polar Regions can be more cooling efficient due to their albedo effects (Sassen and Campbell, 2001). Hence, mid-latitude Ci clouds are assumed to reveal radiative implications varying with season (Sassen and Comstock, 2001; Dupont and Haeffelin, 2008; Campbell et al., 2016; Kienast-Sjögren et al., 2016). Regarding microphysical aspects of the Cirrus clouds, namely ice clouds, they are composed of ice crystals that can present different crystal habits, shapes, orientations, sizes, phases, Ice Water content (IWC), among others, in dependence on their formation mechanism: a) directly from the gas phase (in situ origin), and b) by freezing of liquid father below drops, but uplifted into Ci temperature regimes (liquid origin) (more details, see Krämer et al., 2016). Regardless of the determination of the microphysical features is out the scope of this work, they are directly linked to both the optical and macrophysical properties of Cirrus clouds. Indeed, 'in situ' Cirrus are optically thin and present a lower IWC in comparison with the 'liquid' Cirrus, optically thicker and with a higher IWC. In addition, those Cirrus formation mechanisms depend also critically on the weather situations (convective processes, high pressure frontal systems, jet streams, atmospheric waves, …) (Krämer et al., 2016). Hence, Ci clouds are a weather product; their properties and occurrence can differ over diverse regions of the world.

In general, since Ci clouds form at high altitude levels (typically, from 7 km up to the tropopause), active remote sensing instrumentation, as lidar systems, are widely used for their detection, either deployed in ground-based stations (Sassen and Campbell, 2001; Giannakaki et al., 2007; Seifert et al., 2007; Dupont et al., 2010; Kim et al., 2014; Campbell et al., 2016; Kienast-Sjögren et al., 2016) or aboard space platforms (Sassen et al., 2008; Josset et al., 2012; Zhang et al., 2014; Campbell et al., 2015). Lidars appear as the most suitable instrumentation for high-cloud observations, since they can provide vertical measurements with good vertical and temporal resolutions. The studies conducted by Platt and Sassen (Platt and Dilley, 1981; Sassen et al., 1989) pioneered the studies of Ci clouds with lidars and radiometers and pursued a comprehension on intensive and extensive variables which much affect Ci cloud optical properties. These quantities and the geometric properties of such clouds opened a pathway to explore simulations and models built in order to understand their influence on radiative processes. Understanding the properties and morphology of ice crystals in those clouds allowed the understanding of habits, simple and complex, with geographical variability and under different synoptic conditions (Baum et al., 2011). Also regionally the cloud optical properties have been studied such as in Europe (Dupont et al., 2010; Kienast-Sjögren et al., 2016), North America and Pacific Regions (Hawaii) (Yorks et al., 2011; Campbell et al., 2016), Asian areas (He et al., 2013; Kim et al., 2014), the Mediterranean (Giannakaki et al., 2007) and Indian Sea (Seifert et al., 2007; Das et al., 2009). Therefore, our study represents a significant part of the globe with its own mesoscale processes to formation and circulation of Ci clouds. More recently, in the past ten years, satellites platforms (CERES, CALIPSO, MODIS, CLOUDSAT) (Vaughan et al., 2009; Vaughan et al., 2010; Josset et al., 2012; Guo et al., 2016) have provided important insights on the comprehension of Ci clouds and their role in radiative transfer. Lidar studies devoted to cloud identification and optical properties are of great interest and provide together with CLOUDSAT an important cloud database (Zhang et al., 2014) as the generated results are useful to improve cloud parameterizations in climate models and their validation. In addition, a great effort was made towards correcting multiple scattering effects (Wandinger, 1998), and enhancing the understanding on their temperature dependence (i.e., Garnier et al., 2015).

Moreover, the depolarization factor is a lidar parameter usually used to identify ice phases within the clouds, and then providing an estimate of the internal state of Ci clouds. However, some lidar systems cannot support depolarizing capabilities, hence a thermal threshold for cloud top temperature of <− 37 °C (236 K) (Sassen and Campbell, 2001) or − 38 °C (235 K) (Krämer et al., 2016) (below that value liquid water is absent) is proposed to clearly distinguish Cirrus (ice) cloud presence in lidar profiles (i.e., Campbell et al., 2015; Kienast-Sjögren et al., 2016).

This work describes the methodology for retrieving the macrophysical and optical features of Ci clouds detected by lidar observations, using that temperature threshold of <− 38 °C combined with a modified version of recently proposed procedures (Larroza et al., 2013; Barbosa et al., 2014). Ci clouds features observed in late autumn/early winter season at both subtropical and polar latitudes are analyzed for particular case studies. In addition, their potential latitudinal variability is examined. This study is focused on: (1) classifying the daily cloud features into four Ci categories according to their Cloud Optical Depth (CCOD), as adapted from Sassen et al. (1989) and Sassen and Cho (1992): subvisual-1 (svCi-1, CCOD < 0.03, as a threshold for the visible Ci detection in the zenith), subvisual-2 (svCi-2, CCOD: 0.03–0.1, as a less conservative threshold for visible clouds: Platt et al. (1987) proposed a value of 0.06 instead); semitransparent (stCi, CCOD: 0.1–0.3), and opaque (opCi, CCOD > 0.3) clouds; and (2) analyzing the temperature-related Ci formation with respect to altitude. In order to expand this comparative analysis our ground-based (GB) lidar measurements, as carried out along the day, were evaluated together with the spaceborne lidar CALIOP aboard CALIPSO (Cloud-Aerosol Lidar and Infrared Pathfinder Satellite Observation, www.calipso.larc.nasa.gov) observations (Winker et al., 2009), as performed only once per day. Their similarities and discrepancies are also discussed.

This study strongly encourages the establishment of a long-term Ci clouds monitoring network, and adding future stations to these existing ones, including mid-latitude observations.

2. Methodology

2.1. Ground-based (GB) lidar observations

2.1.1. Stations and lidar systems

Cirrus (Ci) clouds observations were performed in an Antarctic polar station and two subtropical sites. The polar Belgrano II base (BEL, Argentina, 78°S 35°W), managed by the Instituto Antártico Argentino/Dirección Nacional del Antártico (IAA/DNA), is located in deep Antarctica. The two subtropical stations were the Santa Cruz de Tenerife observatory (SCO, Canary Islands-Spain, 28.5°N 16.3°W) and the Metropolitan city of Sao Paulo station (MSP, Brazil, 23.6°S 46.8°W), managed by the Agencia Estatal de Meteorología (AEMET) and the Instituto de Pesquisas Energéticas e Nucleares (IPEN), respectively. Fig. 1 shows the location of all these stations around the world.

Lidar systems deployed at SCO and BEL sites are two Micro Pulse Lidars (MPL) (Campbell et al., 2002), v.3 (MPL-3) and v.4 (MPL-4, including depolarization capability), respectively. MPLs are the standard lidars that are in routine continuous operation (24 h/7 d) within the NASA/MPLNET (MicroPulse Lidar NETwork, mplnet.gsfc.nasa.gov) (Welton et al., 2001), and belong to the Spanish Institute for Aerospace Technology (INTA, Instituto Nacional de Técnica Aeroespacial, www.inta.es/atmosfera), managed in collaboration with the AEMET (Spain) and IAA (Argentina), respectively. The MSP lidar system (SPL) is managed by the IPEN/Centro de Lasers e Aplicaçoes (IPEN/CLA, gescon.ipen.br/leal), and operates within LALINET a.k.a. ALINE (Latin America LIdar NETwork, lalinet.org) (Guerrero-Rascado et al., 2016). Principal features and acquisition settings of each lidar system are shown in Table 1. Lidar signals detected at above 7 km height up to the tropopause are referred to Ci signatures. In the case of the polar Cirrus, in order to avoid Polar Stratospheric Clouds (PSC) contamination (Córdoba-Jabonero et al., 2009, 2013), only PSC-free conditions observed over Belgrano site are considered. Local radiosounding profiles are also used for Cirrus temperature estimation and tropopause levels determination.

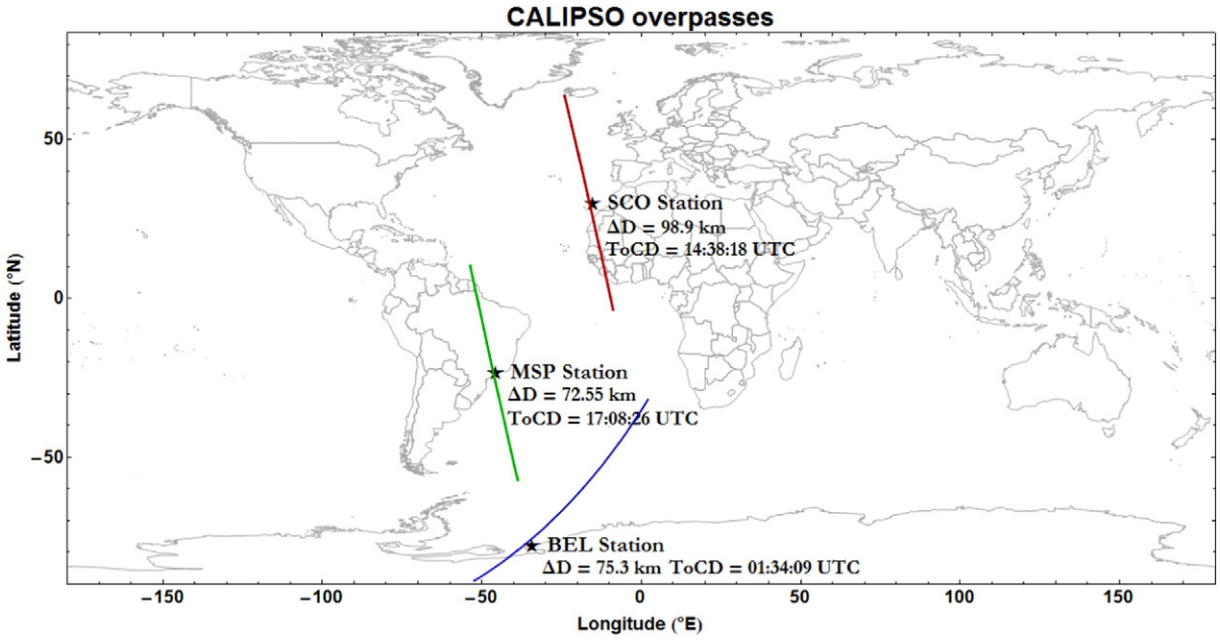

Fig. 1. Map showing the location around the world of the three stations where the lidar measurements were carried out: Santa Cruz de Tenerife/Spain (SCO, 26 November 2009), Metropolitan city of Sao Paulo/Brazil (MSP, 11 June 2007), and the Antarctic Belgrano II base/Argentina (BEL, 22 May 2010). Both CALIPSO trajectories (colour lines) and overpass time (ToCD – Time of Closest Distance) over those stations on the selected Cirrus detection days are also shown. ΔD denotes the closest distance to each station for these days.

Ci clouds were detected between late autumn and early winter seasons over all the stations. In particular, selected Ci cases were observed on 26 November 2009, 11 June 2007 and 22 May 2010, respectively, over SCO, MSP and BEL sites, corresponding to the roughly same seasonal period for both Northern and Southern hemispheres. Their macrophysical and optical parameters were analyzed for these selected case studies along the day, and compared to the single CALIPSO/CALIOP Ci retrievals (the frequency of the CALIPSO overpass over each station is established once per day).

2.1.2. Retrieval of the Ci macrophysical and optical properties

Macrophysical parameters (top and base heights, thickness) and the optical features such as the backscattering ratio profile (BSR, total-to-molecular backscattering coefficient ratio), the Ci Cloud Optical Depth (CCOD), and their Lidar Ratio (LR, extinction-to-backscatter ratio) are retrieved from lidar measurements by using a modified version of the methodology reported in Larroza et al. (2013). Cirrus layer boundaries (top and base heights of the clouds) are determined using a threshold technique, and optical depths (and also lidar ratios) are estimated with an alternative approach of the 'transmission loss' method (Platt, 1973; Young, 1995; Chen et al., 2002; Platt et al., 2002; Yorks et al., 2011). Both CCOD and LR values are also corrected by multiple scattering effects. An overview of the retrieval algorithm is introduced in Appendix A. In particular, an aerosol-free interval is required for determining the calibration constant C (Eq. (3) in Appendix A). Hence, only profiles fulfilling this condition (such an interval is available) were processed, being the altitude range for that calibration: 6–7 km height for the MPL-3 (SCO) and SPL (MSP) lidar systems, and 4–5 km height for the MPL-4 (BEL) lidar (see Table 1). Moreover, uncertainties are estimated for CCOD and LR, being respectively: 16% and 27% for SCO, 6% and 25% for MSP, and 19% and 46% for BEL cases (see Appendix A). The largest uncertainties are found for the polar case, especially for the LR. These BEL estimates are due to a higher occurrence of subvisual Ci clouds is observed over this station (see Sect. 3.1), since errors associated to the retrieved CCOD and LR values for this Ci category are higher than those obtained for others.

2.2. Space-borne CALIPSO/CALIOP observations

CALIOP (Cloud-Aerosol Lidar with Orthogonal Polarization) is a two-wavelength elastic backscatter lidar system aboard CALIPSO satellite (Winker et al., 2009). Its principal features are shown in Table 1.

Table 1
Lidar systems: main features and acquisition settings.

Lidar system (station)	SPL (MSP)	MPL-3 (SCO)	MPL-4 (BEL)	CALIOP/CALIPSO
Routine operation (daily)	2–3 h	24 h	24 h	Once
Lidar Networks	LALINET/ALINE	MPLNET	–	–
Wavelength (nm)	532 (*)	523	527	532 (*)
Energy/pulse (mJ)	150–330	0.007 (max.)	0.010 (max.)	110
Pulse frequency (Hz)	20 (*)	2500	2500	20.25
Eye-safe	No	Yes	Yes	Yes
Depolarization	No	No	Yes	Yes
Raman capability	Yes	No	No	No
Acquisition settings	Vert. res.: 15 m Int. time: 1–2 min	Vert. res.: 75 m Int. time: 1 min	Vert. res.: 75 m Int. time: 1 min	Vert. res.: 30 m (<8.3 km) 60 m (8.3–20.5 km) Horiz. res.: 333 m
Calibration altitude range (km)	6–7	6–7	4–5	–

(*) Used in this work.

CALIPSO Level 1 data (Hostetler et al., 2006) were analyzed in order to retrieve the total attenuated backscatter product and calculate the BSR profiles for each station. A total of 300 BSR profiles were selected in order to obtain a total horizontal range of 100 km (1-profile horizontal resolution is 333 m). Each 15 consecutive profiles of the total attenuated backscatter were averaged in order to obtain a BSR with a horizontal resolution of 5 km. Hence, 20 averaged BSR profiles centered in the coordinates of each lidar station were examined. In particular, CALIPSO overpasses were performed at around 14:38 UTC (daytime), 17:08 UTC (daytime) and 01:34 UTC (nighttime), respectively, over SCO, MSP and BEL stations for those selected days; the closest distance between the CALIPSO ground-track and SCO, MSP and BEL sites was, respectively, 98.9 km, 72.5 km and 75.3 km. Fig. 1 shows CALIPSO trajectory overpasses (colour lines) over those stations on the selected Cirrus detection days, together with the time (ToCD) and closest distance (ΔD) from the station.

CCOD and LR values were obtained from CALIPSO Level 2 Cloud Layer products (Vaughan et al., 2009; Young and Vaughan, 2009) with 5-km horizontal resolution, being retrieved the number of cloud layers detected and their base and top altitudes, as well as their Cloud-Aerosol Discrimination score (CAD). The CALIOP CAD algorithm is used to discriminate between clouds and aerosols using probability distribution functions (PDFs) based on the differences in the optical and physical properties of aerosols and clouds (Liu et al., 2009). The CAD score for clouds is reported in the 5-km cloud products and provides a numerical confidence level for their classification. In this study, Ci layers with a CAD value of 100 (maximal confidence level) were only selected. The CCOD was also used to classify the Ci clouds. Since the CALIPSO overpass over the station is performed for a few seconds, CALIPSO BSR profiles identified in the same Ci-category were averaged. Analysis of Lidar Ratio 532 Selection Method and Cloud Ice/Water Phase Discrimination products (Vaughan et al., 2009; Young and Vaughan, 2009), both from the 5 km Cloud Layer data, confirmed that LR values provided by CALIOP for the three stations studied in this work were obtained by applying the method based on cloud phase (Hu et al., 2009) instead of the 'two-way transmittance' approach (Platt, 1973; Young, 1995; Chen et al., 2002; Platt et al., 2002). Hence, fixed values of 19 ± 10 sr, 25 ± 10 sr, and 22 ± 11 sr are assumed by the CALIOP discrimination algorithm for water, ice and 'unknown' (unable cloud discrimination) clouds, respectively.

Unfortunately, two of the three GB lidars are unable to perform depolarization measurements, lacking the practical estimation of the phase. Instead, Cirrus are distinguished as ice clouds by using the temperature threshold of <−38 °C (close to the also proposed value of −37 °C) at the top of Ci layers for all the stations (Sassen and Campbell, 2001; Campbell et al., 2015; Kienast-Sjögren et al., 2016; Krämer et al., 2016). However, this point will be also analyzed since the ice phase for Ci clouds is also provided by CALIOP.

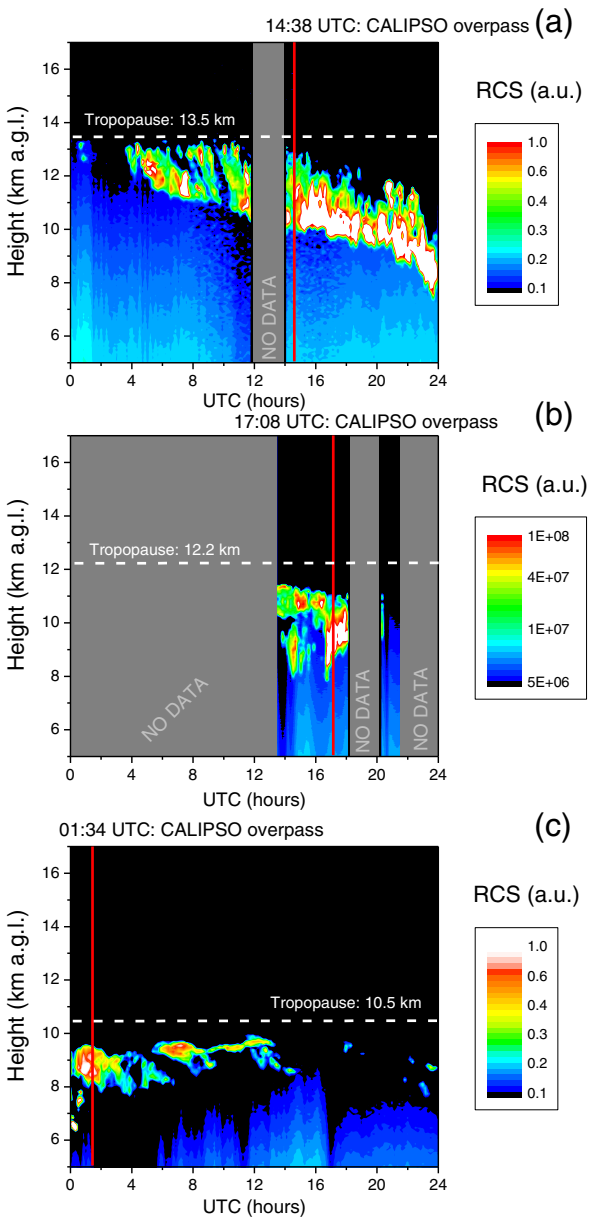

Fig. 2. Daily evolution of the vertical range-corrected signal (RCS) registered by the GB lidar systems located at: (a) SCO site (26 November 2009), (b) MSP site (11 June 2007), and (c) BEL site (22 May 2010). Time of the CALIPSO overpass over each station is also shown (red line) together with the tropopause height-level (dashed white line) for each day. No data are denoted by grey bands.

3. Results

3.1. Optical and macrophysical features of Cirrus clouds

Cirrus clouds are usually observed over the subtropical SCO and MSP sites and the polar BEL station. In this work, particular case studies detected on 26 November 2009 (late autumn), 11 June 2007 (early austral winter) and 22 May 2010 (late austral autumn), respectively, are analyzed. The 1-min/2-min lidar profiles collected along these days are averaged for 10 min to obtain a relatively good signal-to-noise ratio without neglecting potential Cirrus variability. The daily evolution of the Cirrus clouds observed over SCO, MSP and BEL stations is shown in Fig. 2 (panels a, b and c, respectively) in terms of the vertical lidar range-corrected signal (RCS). Ci occurrence is clearly found just below the tropopause height-level for each station (13.5, 12.2 and 10.5 km a.g.l., respectively, for SCO, MSP and BEL sites), as obtained from local radiosounding data.

For those selected days, both the macrophysical parameters determining the extension of Ci layers and their optical properties are retrieved by using the proposed methodology (see Sect. 2.1.2 and Appendix A). Indeed, the vertical backscattering ratio (BSR) $R(z)$ together with both the top and base boundaries of the Ci layers (z^{top} and z^{base}, respectively), their thickness Δz, and their LR and CCOD are determined. Hence, Ci layers are classified into the four selected categories depending on their CCOD (see the Introduction sect.). They are then assembled into groups along the day regarding similar features with prevalence of a given CCOD-type category. Fig. 3 represents the temporal evolution of the vertical BSR $R(z)$ (R^{GBL}) for the Ci clouds observed over the three sites along the day, highlighting the sequential Ci classification found. A label identifying the predominant CCOD-type category for each similar Ci group is also included at the top. In the SCO case, seven Ci groups

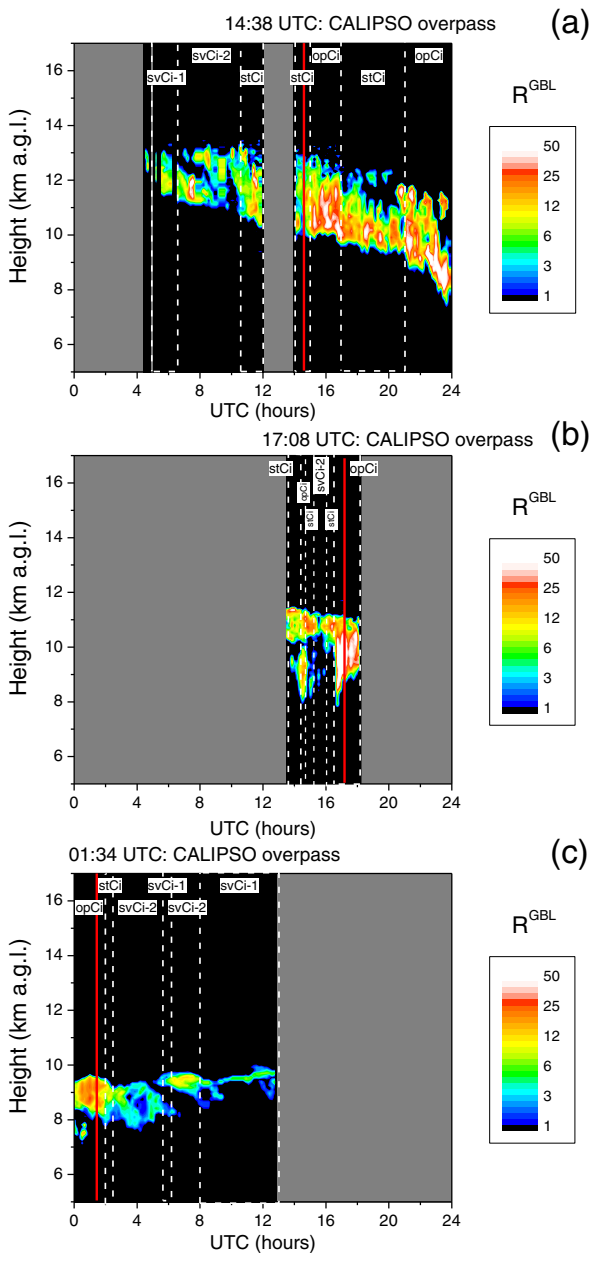

Fig. 3. The same as Fig. 2, but for the vertical BSR $R(z)$ (R^{GBL}). The CCOD-type category (svCi-1, svCi-2, stCi and opCi) identified for each Ci profiling group is also labeled at the top. Time of the CALIPSO overpass over each station is also shown (red line).

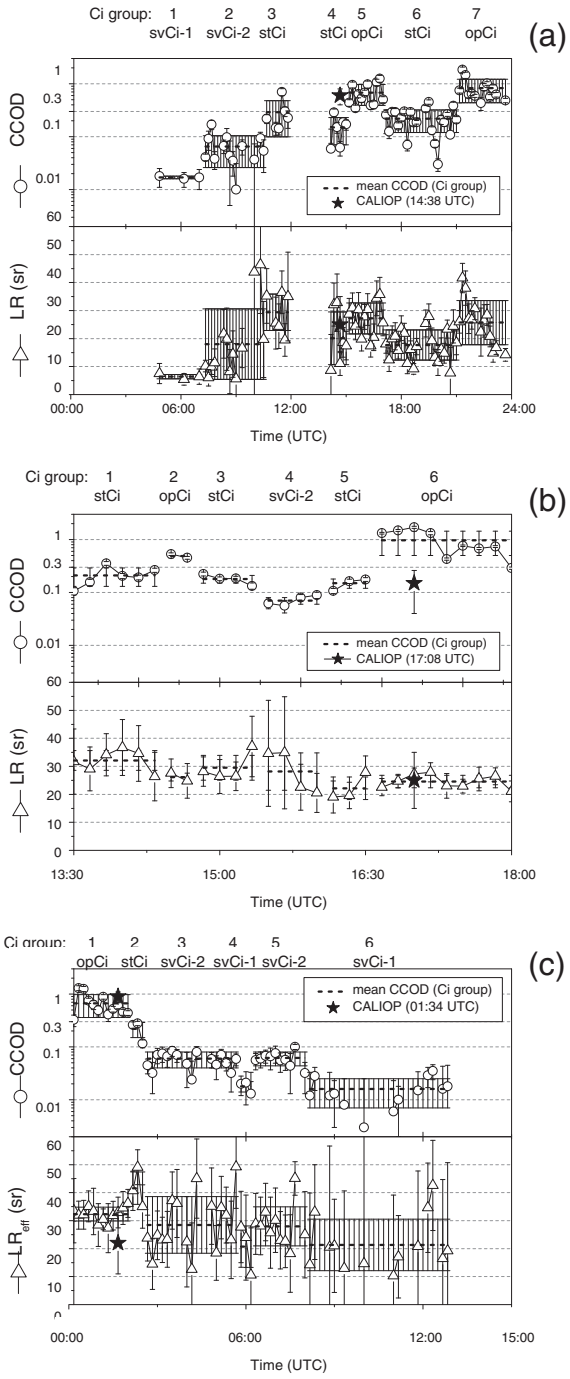

Fig. 4. The same as Fig. 2, but for the effective CCOD (open circles, top panels) and the effective LR (open triangles, bottom panels). Mean values (dashed black lines) together with their standard deviation (error bars) for each Ci group (group number and the predominant Ci category are marked at the top, see text for details) are also shown. Corresponding CALIOP values are also included (black stars).

are selected, being sequentially from svCi-1 (actually, subvisual Cirrus) to opCi clouds (see Fig. 2a), whereas for the MSP case, six are those Ci groups, alternating between stCi and opCi clouds (note that MSP observations were only performed for a few hours). In addition, six Ci groups are analyzed for the BEL case: opCi were observed in the beginning of the day for 2 h, followed by stCi (with low CCOD values nearly within the svCi-2 category) and then alternatively svCi-2 and svCi-1 groups.

CCOD and LR values found for the Ci layers detected along the day over SCO, MSP and BEL stations are shown in Fig. 4 (a, b and c, respectively). In addition, their mean values together with their standard deviation for each selected Ci group are calculated (see Fig. 4, dashed black lines and error bars).

Correspondingly, z^{top}, z^{base} and the thickness Δz found for the Ci layers detected along the day over SCO, MSP and BEL stations are shown in Fig. 5 (a, b and c, respectively, in top panels). Their mean values together with their standard deviation for each selected Ci group are also calculated (see Fig. 5, colored dashed lines and error bars).

Mean values (and their standard deviation) of the optical and macrophysical parameters found for those Ci cloud groups observed over the three stations of this study are shown in Table 2 (CCOD and LR are effective values, see Appendix A). The predominant Ci category (with occurrences higher than 65%) defining each Ci group is also included in Table 2.

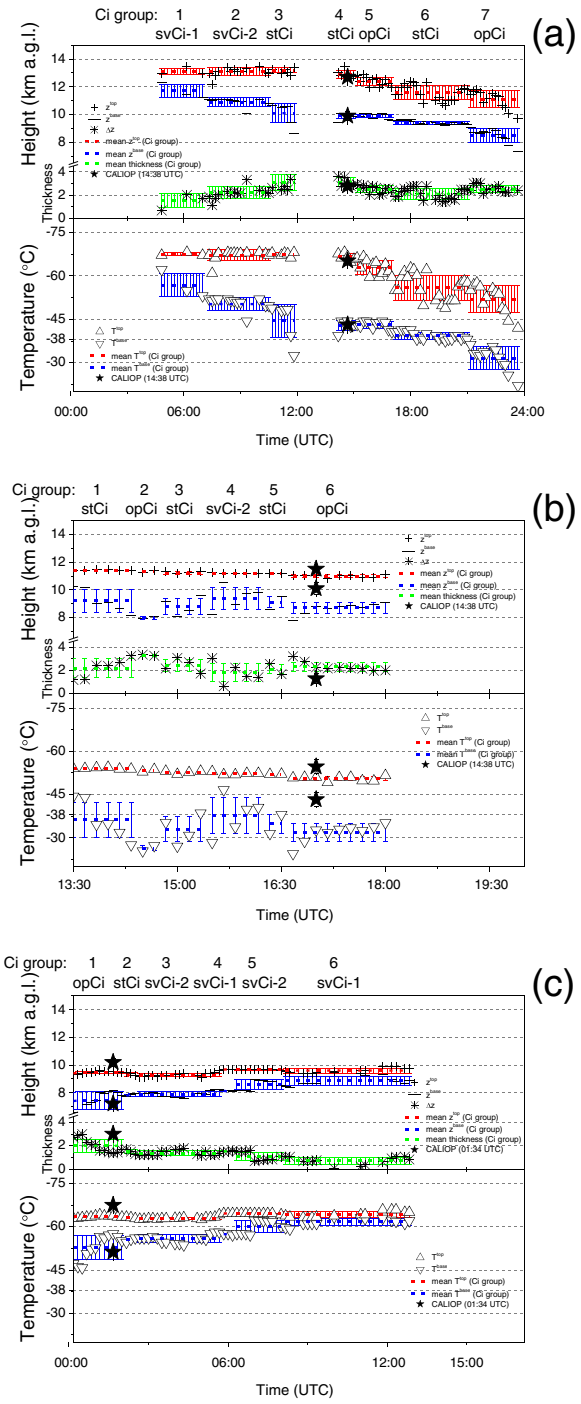

Fig. 5. The same as Fig. 2, but for the Ci layer boundaries, z^{top} ('+' symbols), z^{base} ('−' symbols) and its thickness Δz (cross symbols) (top panels), and their corresponding temperatures, T^{top} (up triangles) and T^{base} (down triangles), respectively, as obtained from local radiosounding data (bottom panels). Mean values (colored dashed lines) together with their standard deviation for each Ci group (group number at the top, see text for details) are also shown. Corresponding CALIOP values are also included (black stars).

Daily SCO features, as also observed in Fig. 3a, present a progressive increase of CCOD values (see Fig. 4a) together to a lowering of the Ci layers (see Fig. 5a). Mean LR values (hereafter, for simplicity, the corresponding standard errors of all the following variables are not shown in the text, and they are only reported in Table 2) are found between 17 and 29 sr for svCi-2, stCi and opCi groups, while rather low LRs (less than 10 sr) are obtained for svCi-1 clouds (see Fig. 4a, and Table 2). z^{base} is ranging from 8.5 to 10 km height for both stCi and opCi, while svCi-1 and svCi-2 are observed no lower than around 11 km height. Besides, stCi and opCi reach z^{top} altitudes between around 11 and 13 km height, while the z^{top} values for svCi-1 and svCi-2 are found higher than 13 km, just below the tropopause height-levels. Additionally, svCi-1 were thinner (1.5 km) than the other Ci groups (2.1–3.1 km, in average) (see Figs. 4a and 5a, and Table 2). In general, results show svCi are found at higher altitudes and present a lower thickness than the two other Ci categories.

In the MSP case, no svCi-1 (actually subvisual Cirrus clouds) were found; and stCi (including svCi-2, selected Ci type within the typical stCi category) and opCi clouds were alternatively observed for a few hours along the day (see Figs. 4b and 5b, and Table 2). Results indicate LR values are ranging closely between 22 and 32 sr for all the Ci categories observed over MSP. In addition, fairly constant mean values are derived for z^{top} (11.0–11.4 km), and variable for z^{base} (9.2–8.0 km), hence the thickness is varying from 1.8 to 3.3 km, in average.

Regarding the polar BEL case, Ci clouds present a CCOD decrease along the day (unfortunately, no data were available from 14:00 UTC on, see Fig. 3c). In overall, Cirrus clouds reached rather similar z^{top} altitudes (9.3–9.7 km height) along the day (svCi are found slightly higher than the other Ci categories), but the thickness was decreasing from 2.0 to 0.7 km (see Fig. 5c, and Table 2). In general, Ci clouds are detected at lower altitudes, as expected at polar latitudes. Mean LR values of 32 sr are found for opCi clouds (Ci group 1, see Table 2), while svCi-1 and svCi-2 present mean LR values of 21 sr and 28–29 sr, respectively. A particular relatively high LR of 42 sr is derived for stCi.

In general, subtropical Ci clouds present relatively close LR values for stCi (as detached in principle in two LR ranges: 18–22 sr and 29–32 sr) and opCi (25–27 sr) categories. In comparison with the subtropical Ci cases, LR values found for polar Ci clouds are rather higher, except they are similar to those found for the svCi-2 category in the MSP case. Large differences (~71%) in LR are found for the svCi-1 category between SCO and BEL sites. Unfortunately, no svCi-1 clouds were observed over MSP on 11 June 2007, hence no other results could confirm the conclusions achieved on the optical and macrophysical properties of the svCi-1 category, likely reflecting their particular ice habits and microphysical internal structure state.

For comparison, CCOD and LR values together with their mean altitude of Ci clouds reported in diverse regions by other authors are shown in Table 3 together with those (daily-averaged) obtained in this work. In average, mean CCOD values are mostly within the opaque category (CCOD: 0.33–0.45), but SW Asia (0.16 ± 0.27) and Indian Sea (0.28 ± 0.29) regions shows a predominance of stCi with a large standard deviation; likewise a high stCi occurrence is found at mid-latitudes in Europe (46–51%) and North America (47/42%, using a fixed LR of 20/30 sr) (see Table 3, and References herein). Hence, mean CCODs obtained in this work are ranging within those reported values: 0.4–0.5 (opCi) and 0.2 (stCi), respectively, for subtropical and polar Ci clouds. Regarding LRs, a higher variability is found in dependence on the region, and the values are ranging from 22 ± 8 sr (North America and Atlantic regions) to 36 ± 20 sr (Mediterranean area), being those retrieved in this work of 21–27 sr and 28 sr, respectively, at subtropical and polar sites (see Table 3, and References herein). In addition, Ci clouds are reported to be observed between 7.5 and 14.5 km height, in general, around the world, likewise our results (9.5–12.5 km) also are found within that altitude interval. Therefore, though specific for our three stations, a good agreement is found for daily-averaged CCOD, LR and Ci altitudes shown in this work; however, the variability of the Ci optical features along the day present large discrepancies.

3.2. Temperature-related Ci formation with respect to altitude

Temperatures of the Ci clouds at their top and base boundaries (T^{top} and T^{base}, respectively) are obtained from local radiosounding profiles.

Table 2
Mean values (±standard deviation) for each selected Ci groups of: effective Cirrus Cloud Optical Depth (CCOD), together to their corresponding predominant Ci-type (svCi-1, svCi-2, stCi and opCi) category (percentage in parenthesis) within each Ci group; effective Lidar Ratio (LR); and both top (z^{top}) and base (z^{base}) heights and thickness (Δz) of Ci layers. In addition, the temperatures of the Ci clouds at their top and base boundaries (T^{top} and T^{base}, respectively), and the tropopause height-level (Z^{trop}) and temperature (T^{trop}) are also included. CALIOP values have also been introduced below the corresponding Ci group in relation to the closest CALIPSO overpass time. N denotes the number of total BSR profiles used in the analysis.

Ci group	CCOD	Predominant Ci-type category (%)	LR (sr)	z^{top} (km)	z^{base} (km)	Δz (km)	T^{top} (°C)	T^{base} (°C)
SCO (26 November 2009) $Z^{trop} = 13.5 \pm 0.3$ km, $T^{trop} = -68.1 \pm 0.4$ °C, $N = 75$								
1	0.017 ± 0.001	svCi-1 (100%)	6 ± 1	13.1 ± 0.2	11.7 ± 0.5	1.5 ± 0.6	−67.5 ± 0.5	−56.8 ± 3.9
2	0.07 ± 0.04	svCi-2 (85%)	17 ± 13	13.1 ± 0.3	10.9 ± 0.3	2.1 ± 0.5	−67.1 ± 1.9	−50.8 ± 2.0
3	0.21 ± 0.09	stCi (67%)	29 ± 7	13.1 ± 0.2	10.1 ± 0.8	3.1 ± 0.8	−67.5 ± 0.6	−44.2 ± 6.2
4	0.15 ± 0.08	stCi (67%)	20 ± 9	12.9 ± 0.3	9.9 ± 0.2	3.1 ± 0.4	−66.6 ± 1.1	−42.9 ± 1.7
CALIOP	0.6 ± 0.2	opCi (95%)	25 ± 10	12.7 ± 0.2	9.9 ± 0.3	2.8 ± 0.3	−65.3 ± 0.4	−43.1 ± 0.5
5	0.7 ± 0.3	opCi (100%)	27 ± 6	12.4 ± 0.3	9.9 ± 0.1	2.5 ± 0.3	−62.9 ± 2.5	−43.1 ± 1.2
6	0.2 ± 0.1	stCi (68%)	18 ± 5	11.6 ± 0.5	9.4 ± 0.1	2.1 ± 0.5	−55.9 ± 4.4	−39.3 ± 1.2
7	0.8 ± 0.4	opCi (92%)	26 ± 8	11.1 ± 0.6	8.5 ± 0.5	2.5 ± 0.3	−51.9 ± 4.7	−31.6 ± 3.9
MSP (11 June 2007) $Z^{trop} = 12.2 \pm 0.3$ km, $T^{trop} = -59.9 \pm 0.9$ °C, $N = 28$								
1	0.21 ± 0.08	stCi (83%)	32 ± 4	11.4 ± 0.0	9.2 ± 0.8	2.2 ± 0.8	−54.1 ± 0.2	−36.3 ± 6.1
2	0.49 ± 0.04	opCi (100%)	26 ± 1	11.3 ± 0.0	8.0 ± 0.1	3.3 ± 0.1	−53.3 ± 0.4	−26.4 ± 0.9
3	0.18 ± 0.03	stCi (100%)	30 ± 4	11.2 ± 0.1	8.8 ± 0.6	2.4 ± 0.5	−52.7 ± 0.4	−33.0 ± 4.4
4	0.07 ± 0.01	svCi-2 (100%)	28 ± 7	11.2 ± 0.0	9.4 ± 0.8	1.8 ± 0.8	−52.3 ± 0.4	−37.9 ± 6.3
5	0.15 ± 0.03	stCi (100%)	22 ± 4	11.2 ± 0.0	9.1 ± 0.4	2.1 ± 0.4	−52.1 ± 0.1	−34.8 ± 3.3
6	1.0 ± 0.5	opCi (89%)	25 ± 2	11.0 ± 0.1	8.7 ± 0.4	2.3 ± 0.4	−50.6 ± 0.8	−31.8 ± 3.0
CALIOP	0.15 ± 0.11	stCi (53%)	25 ± 10	11.5 ± 0.2	10.1 ± 0.4	1.3 ± 0.4	−54.7 ± 2.4	−43.3 ± 2.5
BEL (22 May 2010) $Z^{trop} = 10.5 \pm 0.3$ km, $T^{trop} = -67.6 \pm 0.8$ °C, $N = 57$								
1	0.7 ± 0.3	opCi (100%)	32 ± 3	9.4 ± 0.1	7.4 ± 0.6	2.0 ± 0.6	−63.5 ± 0.4	−52.8 ± 4.3
CALIOP	0.9 ± 0.2	opCi (100%)	22 ± 11	10.2 ± 0.3	7.2 ± 0.2	3.0 ± 0.2	−67.5 ± 0.3	−51.2 ± 0.4
2	0.22 ± 0.07	stCi (100%)	42 ± 6	9.3 ± 0.1	7.8 ± 0.1	1.5 ± 0.2	−63.1 ± 0.2	−55.4 ± 0.6
3	0.06 ± 0.02	svCi-2 (94%)	29 ± 10	9.3 ± 0.1	7.9 ± 0.2	1.4 ± 0.2	−62.9 ± 0.4	−55.9 ± 1.3
4	0.018 ± 0.004	svCi-1 (100%)	21 ± 7	9.7 ± 0.0	8.14 ± 0.04	1.52 ± 0.03	−64.6 ± 0.0	−57.4 ± 0.2
5	0.06 ± 0.02	svCi-2 (90%)	28 ± 7	9.7 ± 0.02	8.6 ± 0.4	1.1 ± 0.4	−64.5 ± 0.1	−60.0 ± 2.2
6	0.016 ± 0.009	svCi-1 (92%)	21 ± 9	9.6 ± 0.2	8.9 ± 0.3	0.7 ± 0.3	−64.2 ± 1.0	−61.6 ± 1.2

Data are also shown in Table 2, together with the tropopause height-level (Z^{trop}) and temperature (T^{trop}).

Fig. 6 shows both the BSR $R(z)$ and temperature profiles (left and right panels, respectively) for the SCO, MSP and BEL cases (panels a, b and c, respectively), displaying also the temperature threshold for ice cloud formation (<− 38 °C). This value is used for distinguishing the water/ice phases of the Ci clouds, below which liquid water does not exist (Campbell et al., 2015; Krämer et al., 2016). In general, z^{top} values indicate that Ci clouds are formed below −38 °C, hence they are all considered as ice clouds. However, differences are clearly observed between subtropical and polar Cirrus clouds. Whereas polar Ci layers are completely inside the total ice phase temperature band ($T < -38$ °C), the subtropical ones are partially within this ice threshold band, mainly remarkable for the opCi category. In particular, subtropical svCi-1 and svCi-2 clouds are formed at higher altitudes and lower temperatures (in general, <− 45 °C) than the other stCi and opCi categories (see Fig. 6a and b, and Table 2). Likewise, all the Ci clouds present for the BEL case, svCi-1, svCi-2, stCi and opCi, form at lower temperatures (<− 52 °C) than those for both the subtropical cases, as expected, despite they are detected at lower altitudes. Indeed, this is related to the fact that the polar tropopause is found at lower altitudes (around 10.5 km height in our polar case).

These temperature-related features of the Ci clouds can affect, indeed, their internal state, and hence the differences observed in the LR, especially for the svCi-1, between the subtropical and polar cirrus clouds can be explained in the basis of different temperature regimes

Table 3
Values reported in the literature for CCOD (or predominant Ci category, in average), LR and mean altitude for Ci clouds. For comparison, daily mean values obtained in this work are also included.

Location	CCOD (predominant Ci category	LR (sr)	Mean altitude (km)	Reference
Pacific area	0.44 ± 0.27	25 ± 10	13 ± 1	Yorks et al. (2011)
Central Asia	0.33 ± 0.29	28 ± 15	14.5 ± 1.7	He et al. (2013)
SW Asia	0.16 ± 0.27	23 ± 16	14.0 ± 2.0	Das et al. (2009)
Seoul (Korea)	0.42 ± 0.39	25 (*)	10.6 ± 1.2	Kim et al. (2014)
Indian Sea	0.28 ± 0.29	31 ± 10	12.5 ± 1.5	Seifert et al. (2007)
Australia		27 ± 7		Thorsen and Fu (2015)
North America			10.0	Sassen and Campbell (2001)
North America	0.35 ± 0.27	31 ± 11	13 ± 2	Yorks et al. (2011)
North America		22 ± 7		Thorsen and Fu (2015)
North America	stCi (47/42%)	20/30 (*)	7.5–14.5	Campbell et al. (2016)
Central America	0.33 ± 0.23	26 ± 10	14.5 ± 2.5	Yorks et al. (2011)
South America			9.0	Lakkis et al. (2009)
Atlantic region	0.45 ± 0.26	22 ± 8	13 ± 1	Yorks et al. (2011)
Europe	0.12–0.17 stCi (46–51%)	5–40 (**)	10.3–10.7	Kienast-Sjögren et al. (2016)
Mediterranean area	0.33 ± 0.25	36 ± 20	10 ± 1	Giannakaki et al. (2007)
Global Satellite - Over Sea		33 ± 5		Josset et al. (2012)
North Atlantic – Africa (subtropical SCO)	0.4 ± 0.4	21 ± 10	12.5 ± 0.8	This work
South America – Atlantic coast (subtropical MSP)	0.5 ± 0.5	27 ± 5	11.2 ± 0.1	This work
Antarctica (BEL)	0.2 ± 0.3	28 ± 9	9.5 ± 0.2	This work

(*) Assumed fixed values.
(**) LR range used in the retrieval.

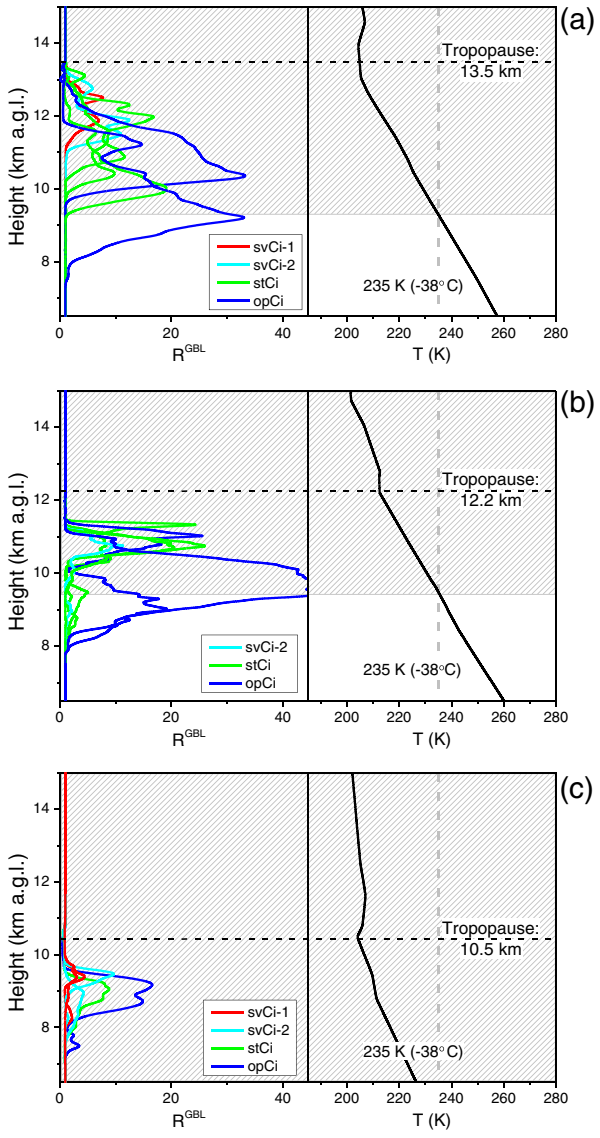

Fig. 6. (Left panels) Cirrus clouds observed over (a) SCO site on 26 November 2009, (b) MSP site on 11 June 2007, and (c) BEL site on 22 May 2010 in terms of BSR profiles derived from GB lidar measurements (R^{GBL}), as grouped depending on the predominant Ci-type category: Ci clouds are detached into svCi-1 (red), svCi-2 (cyan), stCi (green), and opCi (blue). (Right panels) Temperature profiles obtained from local radiosoundings over each station. The temperature threshold for ice cloud formation of −38 °C (235 K) is also marked (grey dashed line), delimitating the 'ice zone' by dashed bands. BSR error bars were removed for clarity.

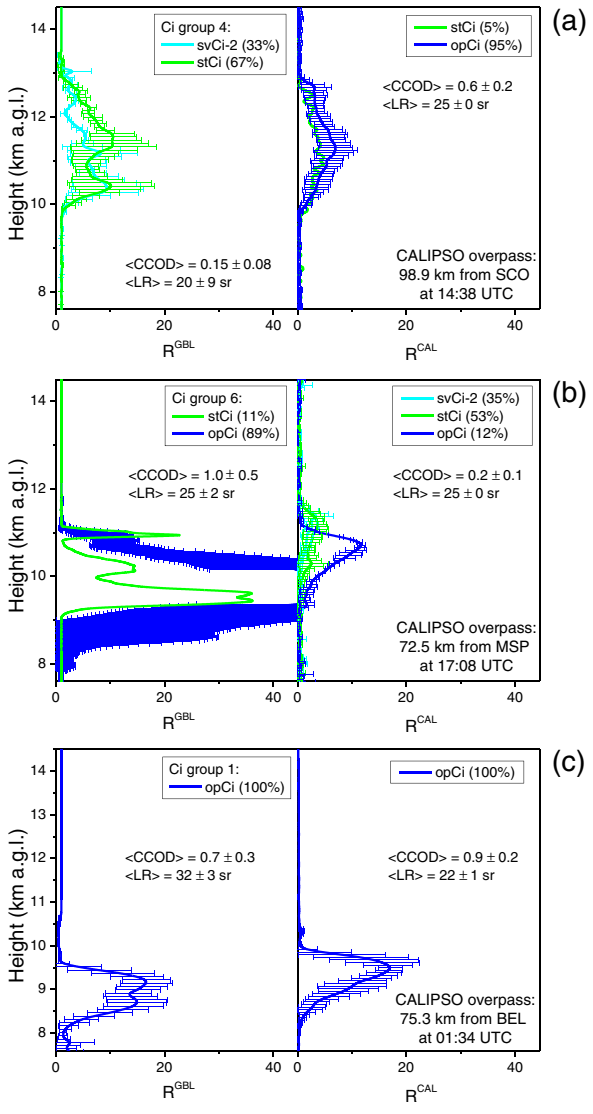

Fig. 7. Near real-time observations of Ci clouds observed at the closest time to the CALIPSO overpass (distance from the station and time are also indicated) over (a) SCO site on 26 November 2009, (b) MSP site on 11 June 2007, and (c) BEL site on 22 May 2010, in terms of BSR profiles derived from GB lidar (R^{GBL}) (left) and CALIOP (R^{CAL}) (right) measurements (see text for details). The corresponding Ci group is detached into: svCi-1 (red lines), svCi-2 (cyan lines), stCi (green lines), and opCi (blue lines) categories, showing their resultant percentage within the Ci group. Mean values of CCOD and LR for the Ci group are also included.

for Ci formation (Krämer et al., 2016). In addition, the multiple scattering factor (η), under those different temperature-related Ci formation processes, can experience a dependence on the temperature (Garnier et al., 2015), hence affecting the retrieved LR values, and also the CCOD, of the Ci layers in comparison with the single constant η factor applied in this work (see Appendix A). Unfortunately, two of the three lidar systems used in this study were unable to perform depolarization measurements, hence no estimation on the microphysical features of the Ci layers can be extrapolated from these kind of results. In the next section, the cloud phase provided by CALIPSO will be examined.

3.3. Comparison between the GB lidar and CALIPSO/CALIOP retrievals

It should be taken into account that GB lidar measurements are performed along the day, whereas CALIOP observations are conducted for a few seconds over each station during the CALIPSO overpass.

Results obtained from GB lidar measurements (10-min averaged profiles) at both subtropical (SCO/MPL-3 and MSP/SPL) and polar (BEL/MPL-4) sites are compared against CALIPSO/CALIOP retrievals (see Sect. 2 for details), based on near real-time measurements for 1 h around the closest time of CALIPSO overpasses over each station. Fig. 7 shows the GB BSR profiles within the Ci group closer in time to the CALIPSO overpass (left panels), and CALIOP observations corresponding to the 5-km horizontal resolution profiles (right panels), as averaged depending on the assigned Ci-type category (Ci occurrence percentage is also included). In addition, mean values of the optical parameters (CCOD, LR) and macrophysical features (z^{top}, z^{base}, Δz) of Ci layers retrieved by CALIOP algorithms, and related to the data shown in Fig. 7, are displayed in Figs. 4 and 5 (black stars), respectively. Table 2 also includes these CALIPSO/CALIOP mean values (below the corresponding Ci group in relation to the closest CALIPSO overpass time). Fig. 8 illustrates the CALIPSO overpass in the proximity of each station in terms of the

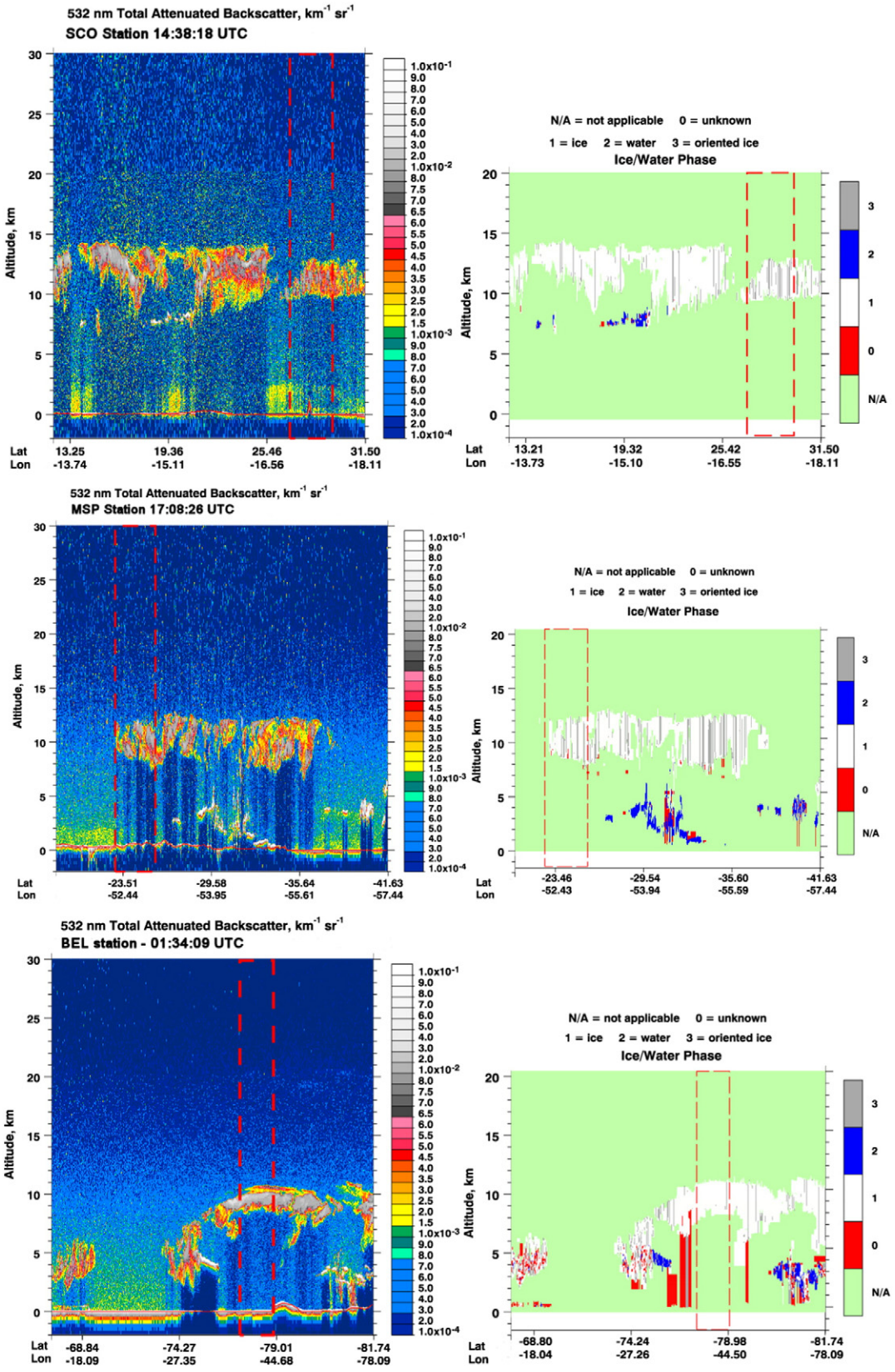

Fig. 8. (Left) CALIPSO overpass in the proximity of each station: (a) SCO, (b) MSP and (c) BEL, in terms of the 532-nm total attenuated backscatter along its trajectory (the nearest position to the station is enclosed by red dashed lines). (Right) The same as in Fig. 8-left, but in terms of the water/ice cloud phase (denoted in the legend) for the corresponding observed Ci clouds.

532-nm total attenuated backscatter along its trajectory, showing also its nearest position to the station (red dashed lines), and the water/ice cloud phase (see the legend) for the corresponding observed Ci clouds.

Over SCO site, opCi clouds are mostly observed by CALIOP; stCi are only identified in a 5% of the Ci layers detected, and no svCi-1 and svCi-2 are found (see Fig. 7a-right). Hence, mean values of CCOD are rather higher (0.6 ± 0.2) than those reported by the GB lidar (MPL-3) (0.15 ± 0.08), observing mainly stCi (67%) at that time (see Fig. 7a-left). Since CALIOP assumed a LR value of 25 ± 10 sr (daytime measurements, and Ci clouds flagged as 'ice' using the CALIOP cloud phase method, see Sect. 2.2 and Fig. 8a), the satellite sensor was unable to discriminate subvisual Cirrus clouds (i.e., svCi-1). Regarding LR, GB retrievals report a mean value of 20 ± 9 sr, slightly lower than that for CALIOP (25 sr) (see Fig. 4a-bottom). Otherwise, Ci clouds are found at similar altitudes (between around 10 and 13 km height) (see Fig. 5a-top). Those discrepancies found in CCOD and LR (though less pronounced) can be likely related to the rather large distance of the CALIPSO overpass from the station (98.9 km), since the diversity on the Ci optical features is clearly significant regarding the daily variability found for the Ci clouds detected over SCO site. In fact, CALIOP values are in a closer agreement to those obtained for the Ci clouds observed later over SCO (i.e., mean CCOD of 0.7 ± 0.3 and LR of 27 ± 6 sr are retrieved for the following Ci group, see Table 2). This can be related to the irregular extension and inhomogeneity of the Ci clouds over that study area.

For the MSP case, both stCi and opCi occurrence is observed by the GB lidar (SPL) and CALIOP, but in a different proportion: mostly opCi (89%) and stCi (53%) are identified by SPL and CALIOP (also svCi-2, 35%), respectively (see Fig. 7b). This result is reflected in the mean CCOD calculated from SPL (1.0 ± 0.5) and CALIOP (0.2 ± 0.1) retrievals. A mean LR of 25 ± 2 sr is reported from the GB measurements, in agreement with that value assumed by CALIOP (25 sr, and Ci clouds were labeled as 'ice', see Sect. 2.2 and Fig. 8b). In addition, Ci clouds are also detected at similar top altitudes (around 11.5 km height), but they are thinner (1.3 km, in average) than those observed from the MSP site (2.3 km, in average). As stated before for the SCO case, differences found in CCOD values derived from GB and space-borne observations can be also associated to the CALIPSO overpass distance from the MSP station (72.5 km), despite it is closer than from SCO. The Ci-category variability is also observed over MSP (despite GB observations were only performed for a few hours), and CALIOP retrievals are closer to those derived for the Ci clouds observed earlier over MSP (i.e., mean CCOD of 0.15 ± 0.03 and LR of 22 ± 4 sr are retrieved for the previous stCi group, see Table 2).

In the polar case, only opCi clouds are identified by CALIOP, retrieving mean values of 0.9 ± 0.2 for CCOD and 22 ± 11 sr for LR (see Fig. 7c-right). In comparison, at the closest time of CALIPSO overpass over BEL station, GB measurements (MPL-4) indicate only opCi occurrence (100%) (see Fig. 7c-left), obtaining mean CCOD and LR values of 0.7 ± 0.3 and 32 ± 3 sr, respectively. No svCi-1, svCi-2 and stCi are found in both cases. Hence, the CALIOP derived values for CCOD and LR are close to and lower than, respectively, those retrieved from MPL-4 data. Despite the LR values for the three cases, SCO, MSP and BEL stations, were retrieved by the cloud phase method used by CALIOP (see Sect. 2.2) instead of the two-way transmittance approach, as used in this work (see Appendix A), no large discrepancies are obtained in the LR values derived from GB and CALIOP retrievals. Regarding the top altitudes found for Ci clouds, whereas base heights are found at similar altitudes (7.2–7.4 km height), CALIOP detected Ci clouds slightly higher (around 10.2 km height) than those observed by the GB lidar system (around 700 m below) (see Fig. 5c-top). Those differences found in optical and macrophysical features between CALIOP and GB observations (less pronounced for CCOD) are smaller in comparison with the subtropical cases, despite the also large distance of the CALIPSO overpass from the station (75.3 km). These results can point out the lower atmospheric variability occurred in polar areas than at subtropical latitudes.

As exposed before (see Sect. 3.2), unfortunately, two of the three GB lidar systems are unable to use depolarization capabilities, hence an estimate of the microphysical state of Ci clouds is unavailable. Instead, the ice/water phase provided by CALIOP is analyzed.

Subtropical Ci clouds present phases identified as a mixture of ice and oriented ice particles (see Fig. 8a and b); the polar case corresponds mostly to ice clouds (a few CALIOP profiles were 'unknown phase' flagged). Indeed, the differences found in LR between subtropical and polar Ci clouds, mainly for the svCi-1 category (rather low LR values were found for subtropical Ci, likely inferring a higher presence of horizontally-oriented crystals in the cloud) (Krämer et al., 2016), can be related to the ice phase of the Ci clouds in each case (higher LR values are obtained for polar clouds showing only pure ice phases and no mixtures). However, this point was unable to be addressed within the context of the present study, but it could be examined on a future work.

4. Conclusions

Cirrus (Ci) clouds were detected in late autumn/early winter season by GB lidar systems deployed in three stations located at both subtropical and polar latitudes. Their properties (in particular, macrophysical and optical features) were derived by using lidar measurements in combination with a retrieval algorithm (also described in this work, see Appendix A). Subtropical and polar Ci clouds features were examined for particular case studies, and compared to CALIPSO/CALIOP data. The BSR profiles and the top and base boundaries of the Ci layers together to their Cirrus Cloud Optical Depth (CCOD) and Lidar Ratio (LR) were derived. In addition, temperatures at the top and base heights of the Ci clouds were also obtained from local radiosoundings to confirm pure ice Ci clouds occurrence using a given temperature top threshold (this value is lower than −38 °C in this work) (Kienast-Sjögren et al., 2016; Krämer et al., 2016).

Ci clouds observed along the day were assembled in groups based on their predominant CCOD. Hence, these Ci groups were classified according to four CCOD-based categories: svCi-1 (CCOD < 0.03), svCi-2 (CCOD: 0.03–0.1, as a less conservative threshold for visible clouds); stCi (CCOD: 0.1–0.3), and opCi (CCOD > 0.3). Ci layers were studied in terms of their retrieved LR values and both top and base boundaries for each Ci category. Furthermore, the relation with the temperature at their top and base heights was also analyzed.

In general, polar Ci clouds present LR values (svCi-1: 21 sr, svCi-2: 28–29 sr, stCi: 42 sr, and opCi: 32 sr) higher than those for subtropical Ci clouds (svCi-1: <10 sr, svCi-2: 17–29 sr, stCi: 18–32 sr, and opCi: 25–27 sr) regarding each Ci category. In addition, LR values derived for svCi-1 (the actual namely subvisual clouds) are lower than those retrieved for stCi and opCi clouds, independently on the latitude. These results are likely inferring differences in the internal state of Ci clouds, and hence the plausible diversity in their microphysical properties, depending on their Ci category and regional detection.

Regarding Ci clouds altitudes, in general, subtropical opCi are observed lower than svCi-1 clouds, with top values ranging, respectively, from 11 to 13 km height, nearby the tropopause over each station. In particular, svCi-1 are located closer to the tropopause level (0.5 km below) than opCi (1.2 km). However, Polar Cirrus are detected, in general, at lower altitudes, as expected in Polar Regions, but all the Ci categories are found at similar heights, likely due a higher stability of the polar atmosphere.

In general, Ci clouds are observed to be vertically-distributed in relation with the temperature (the higher altitudes the lower temperatures) in dependence on the Ci category. Indeed, svCi-1 clouds form at lower temperatures at both latitudes and hence are detected at higher altitudes than the other Ci categories (decreasingly in altitude, svCi-2, stCi and opCi are observed), providing to some extent evidence on the thermodynamic structure of the atmosphere. In particular, the tropopause over MSP is lower than over SCO on the selected days, hence Ci clouds were detected at lower altitudes and higher Ci top temperatures

were reported; in fact, svCi-1 were unobserved over MSP site. In addition, the temperature regimes for Ci formation likely influence the internal state of the Cirrus clouds, their internal ice habits (Krämer et al., 2016), and hence affect the LR of the Ci layer. These results are in agreement with the variability observed in LR values retrieved for the Ci categories detected over the three stations of this study, especially the differences found in LR for svCi-1 between the subtropical (SCO) and polar (BEL) Ci cases. Moreover, a higher svCi occurrence is also observed over the polar station, as expected, since svCi clouds form at lower temperatures.

In comparison with CALIOP data, Ci clouds are observed at similar altitudes over each GB station (around 10–13 km height). However, differences are found mostly in CCOD values for subtropical Ci clouds, whereas LR values are in a closer agreement. Those discrepancies are likely related to the rather large distance of the CALIPSO overpass from the station (98.9 and 72.5 km for SCO and MSP site, respectively), since the diversity on the Ci optical features is clearly significant regarding the daily variability found for the Ci clouds detected over SCO and MSP. In the polar case, the differences found in optical and macrophysical features between CALIOP and BEL observations are smaller, though higher for the LR retrieved values, in comparison with the subtropical cases, despite the also large distance of the CALIPSO overpass from the station (75.3 km). These results can point out the lower atmospheric variability occurred in polar areas than at subtropical latitudes. However, those discrepancies can also reflect the fact that a fixed value of 25 sr is assumed in CALIOP inversion retrievals for CALIPSO daytime observations over the subtropical SCO and MSP stations, whereas a LR value of 22 ± 11 sr is used in the polar case (CALIPSO overpassing over BEL site is at nighttime) (Young and Vaughan, 2009).

Moreover, a good agreement is found for daily-averaged CCOD and LR values and Ci top heights in comparison with values reported by other authors in different regions; however, the variability of the Ci optical features along the day present large discrepancies. Indeed, despite only one case study of Ci clouds detected over the three stations was examined in this work, results show the relatively high diversity of Ci clouds properties along the day, with implications for their daily radiative effect estimation (Dupont and Haeffelin, 2008; Das et al., 2009; Campbell et al., 2016; Kienast-Sjögren et al., 2016). This is relevant in comparison with the low frequency of the CALIOP/CALIPSO overpassing over each station, limited to once per day, either at daytime or nighttime, for climatological implications of Ci clouds.

Even though ancillary suitable data, as temperature profiles and precipitable water content in the clouds, are required to better comprehend the Ci formation mechanism, this work gives the possibility to further explore the differences in Ci cloud formation at mid-latitudes in comparison with the Ci features found at subtropical and polar regions. Moreover, the subtropical lidar systems employed in this study were not perfectly suitable to inspect 'stratospheric cirrus clouds' as related elsewhere in the literature (Iwasaki et al., 2015).

Furthermore, despite these results are specific for those particular Ci cases analyzed, they also show the importance to encourage the establishment of a Ci cloud monitoring network in order to evaluate the temporal (daily) and spatial (latitudinal) variability of the optical and macrophysical properties of the Ci clouds, and hence to determine their radiative impact and estimate the particular thermodynamic state of the atmosphere. Indeed, a larger dataset of Ci clouds, detected over the stations of this study, adding others to the existing ones in the future, including also mid-latitude observations, must be analyzed in order to validate to some extent those similarities and discrepancies found in this work. In addition, in case depolarization measurements can be performed, an estimate of the microphysical features can be also achieved. Therefore, this would be an essential task for the near future. Moreover, such considerations can be useful for both latitude-dependent Ci properties assimilation into climate models and evaluation of space-borne lidar observations of Ci clouds, especially for the future ESA/Copernicus-Sentinel and ESA/EarthCARE missions.

Acknowledgements

This work is supported by the Spanish Ministerio de Economía y Competitividad (MINECO) under grant CGL2014-55230-R (AVATAR) and the INTA project IGE03004. Authors wish to acknowledge the entire CALIPSO team for their substantial contributions and for the data obtained from the NASA Langley Research Center (LRC). The MPLNET project is funded by the NASA Radiation Sciences Program and Earth Observing System. Authors thank the Department of Atmospheric Science of the University of Wyoming for the radiosounding data profiles. Authors also are grateful to the staff of all the stations responsible for instrumentation maintenance and support, and M. Yela as manager of INTA Antarctic program at the Belgrano II base. F.J.S. Lopes and C. Córdoba-Jabonero thank the Fundação de Amparo à Pesquisa do Estado de São Paulo (FAPESP) for their support under grants 2011/14365-5 and 2013/11836-2, respectively.

Appendix A

A.1. General background in lidar terminology

The lidar equation defines the relation between the backscattered signal $P(r)$ registered by a lidar system and the atmospheric optical properties associated to both the molecular (Rayleigh) component and aerosols. This equation is expressed as

$$P(r) = \frac{C \cdot E \cdot \beta(r) \cdot T^2(r)}{r^2}, \tag{1}$$

where $P(r)$ is the backscattered signal registered by the lidar system (once corrected by all the intrinsic and specific instrumental variables of the system), r is the range, or the height in case the lidar is zenithally pointing as usual, C is the calibration constant (dependent on the instrument), E is the laser pulse energy, and $\beta(r)$ is the total backscatter coefficient ($=\beta_m(r)+\beta_a(r)$, being $\beta_m(r)$ the backscatter coefficient for molecules (Rayleigh) and $\beta_a(r)$ for aerosols (in m^{-1} sr^{-1}). $T(r)$ is the transmittance of the atmosphere ($=T_m(r)\times T_a(r)$, being $T_m(r)$ the transmittance due to molecules (Rayleigh) and $T_a(r)$ that due to aerosols, in a two-component scenario), and is expressed as

$$T(r) = \exp\left[-\int_0^r [\sigma_m(r\prime) + \sigma_a(r\prime)] \cdot dr\prime\right], \tag{2}$$

where $\sigma_m(r)$ is the molecular extinction coefficient (in m^{-1}) and $\sigma_a(r)$ is the extinction coefficient of the aerosols (in m^{-1}).

The energy- and range-corrected lidar signal (in short, range-corrected signal, RCS) $P_r(r) = P(r)\frac{r^2}{E}$ can be expressed as

$$P_r(r) = C \cdot \beta^{att}(r) \tag{3}$$

where $\beta^{att}(r) = \beta(r) \cdot T^2(r)$ is the so-called total 'attenuated' backscatter coefficient. The calibration constant C in Eq. (3) can be estimated by using an aerosol-free (only the molecular contribution is considered) height-interval ($r_m : r_1 \ldots r_i$, called Rayleigh fitting interval hereafter) in the lidar RCS, where the assumption of $\beta_a(r) = 0$ (and also $\sigma_a(r) = 0$) at r_m altitudes could be fulfilled. Hence, Eq. (3) can be written as

$$P_r(r_m) = C \cdot \beta^{att}(r_m) = C \cdot \beta_m(r_m) \cdot \exp\left[-2 \cdot \int_0^{r_m} \sigma_m(r\prime) \cdot dr\prime\right] \tag{4}$$

along the Rayleigh fitting interval r_m. Both the molecular backscatter $\beta_m(r_m)$ and extinction $\sigma_m(r_m)$ coefficients can be easily obtained from radiosounding data (pressure and temperature profiles) at that selected Rayleigh fitting interval ($r_m : r_1 \ldots r_i$). Finally, C is calculated by averaging all those values $\left({}^{P_r(r_i)}/_{\beta_m(r_i)\cdot \exp[-2\cdot\int_0^{r_i}\sigma_m(r\prime)\cdot dr\prime]}\right)$ within the selected Rayleigh fitting interval ($r_m : r_1 \ldots r_i$).

The backscattering ratio (BSR) $R(r)$ is defined as the ratio between the total backscattering $\beta(r)$ and the molecular $\beta_m(r)$ coefficients, i.e.,

$$R(r) = \frac{\beta(r)}{\beta_m(r)} = \frac{\beta_m(r) + \beta_a(r)}{\beta_m(r)}. \quad (5)$$

From Eq. (5), and by using the "attenuated" backscatter coefficient $\beta^{att}(r) = \beta(r) \cdot T^2(r)$, the corresponding so-called "attenuated" backscatter ratio $R^{att}(r)$ can be also be defined as

$$R^{att}(r) = R(r) \cdot T^2(r) = \frac{\beta(r)}{\beta_m(r)} \cdot T^2(r) = \frac{\beta^{att}(r)}{\beta_m(r)}. \quad (6)$$

Hence, $R^{att}(r)$ can be "experimentally" obtained by using Eq. (3), as follows

$$R^{att}(r) = \frac{P_r(r)}{C\beta_m(r)}, \quad (7)$$

once C is estimated by using Eq. (4), and the $\beta_m(r)$ and $\sigma_m(r)$ coefficients are obtained from radiosounding data.

A.2. Calculation of the Ci cloud optical depth (CCOD) and the Lidar Ratio (LR)

A.2.1. Ci cloud optical depth τ_c (CCOD)

By using Eq. (2), Eq. (6) can be written as

$$R^{att}(r) = R(r) \cdot \exp\left[(-2) \cdot \int_0^r [\sigma_a(z) + \sigma_m(z)] \cdot dz\right]. \quad (8)$$

In the case of Ci clouds as the unique aerosols present, $\sigma_a(z) = \sigma_c(z)$, and $\sigma_m(z)$ can be assumed negligible as compared to $\sigma_c(z)$ for a cloud layer. Hence, Eq. (8) can be expressed as

$$R^{att}(z_i) = R(z_i) \cdot \exp\left[(-2) \cdot \int_{z_1}^{z_i} \sigma_c(z) \cdot dz\right], \quad (9)$$

where $\sigma_c(z)$ is the extinction coefficient of the Ci cloud, and z_i represents the range of altitudes with Ci presence, i.e. the cloud layer $z_L: z_1 < z_i < z_2$, being z_1 and z_2 the cloud base and top height boundaries, respectively. Determination of z_1 and z_2 will be described in Sect. A4. Hence, the Ci cloud optical depth (CCOD) $\tau_c(z_L)$ of the Cirrus layer z_L is expressed as

$$\tau_c(z_L) = \int_{z_1}^{z_2} \sigma_c(z) \cdot dz, \quad (10)$$

being the transmittance $TT(z_L)$ of the Cirrus layer

$$TT(z_L) = \exp[-\tau_c(z_L)]. \quad (11)$$

In order to estimate $\tau_c(z_L)$ the so-called "Transmittance Method" (TM) (Platt, 1973; Young, 1995; Chen et al., 2002; Platt et al., 2002) is used. This method is based on the selection of two cloud-free (Rayleigh) height-ranges, below ($z < z_1$) and above ($z > z_2$) the cloud layer, where $R^{att}(z)$ can be estimated. That is, $R^{att}(z)$ can be expressed by using Eqs. (9)–(11) as follows

$$R^{att}(z < z_1) = R(z < z_1) \quad (12)$$

and

$$R^{att}(z > z_2) = R(z > z_2) \cdot TT^2(z_L), \quad (13)$$

where $z_1 < z_L < z_2$, as mentioned before. Then, dividing Eq. (13) by Eq. (12), and in the basis of these two height-ranges ($z < z_1$) and ($z > z_2$) are Rayleigh (cloud-free) assumed, $R(z < z_1) = R(z > z_2)$, and the expression for $TT(z_L)$ can be written as

$$TT(z_L) = \sqrt{\frac{R^{att}(z > z_2)}{R^{att}(z < z_1)}}. \quad (14)$$

Hence, from Eq. (11), the CCOD $\tau_c(z_L)$ of the Cirrus layer z_L can be "experimentally" determined, that is,

$$\tau_c(z_L) = -\ln[TT(z_L)] = -\frac{1}{2} \cdot \ln\left[\frac{R^{att}(z > z_2)}{R^{att}(z < z_1)}\right]. \quad (15)$$

A.2.2. Lidar Ratio LR

One of the most relevant parameters in lidar terminology is the Lidar Ratio $LR(r)$, defined as the ratio between the extinction and backscatter coefficients, i.e.,

$$LR(r) = \frac{\sigma(r)}{\beta(r)}. \quad (16)$$

This parameter is dependent on the composition, shape and size, among other properties, of the particles, and then widely used for aerosol-type classification from lidar measurements.

In the case of Ci clouds, LR is expressed as follows

$$LR(z_L) = \frac{\sigma_c(z_L)}{\beta_c(z_L)}, \quad (17)$$

where $\sigma_c(z_L)$ and $\beta_c(z_L)$ are, respectively, the extinction and backscatter coefficients for the Ci cloud, where z_L represents the cloud layer: $z_1 < z_i < z_2$. For simplicity, Ci clouds can be considered as a homogeneous layer, and hence $LR(z_L) = LR$, i.e., LR is assumed to be a height-independent parameter within each cloud layer.

Replacing $\beta_a(r)$ by $\beta_c(z_L)$ in Eq. (5), $\sigma_c(z_L)$ can be expressed by using Eq. (17) as

$$\sigma_c(z_L) = LR \cdot \beta_c(z_L) = LR \cdot \beta_m(z_L) \cdot [R(z_L) - 1]. \quad (18)$$

Hence, Eq. (10) can be expressed as

$$\tau_c(z_L) = \int_{z_1}^{z_2} \sigma_c(z) \cdot dz = LR \cdot \int_{z_1}^{z_2} \beta_m(z) \cdot [R(z) - 1] \cdot dz. \quad (19)$$

Finally, LR can be directly calculated from Eq. (19):

$$LR = \frac{\tau_c(z_L)}{\int_{z_1}^{z_2} \beta_m(z) \cdot [R(z) - 1] \cdot dz} \quad (20)$$

where $\beta_m(z)$ can be estimated from radiosounding data, and $\tau_c(z_L)$ by using Eq. (15). Just the BSR $R(z)$ must be also known to determine the LR. An 'a priori' LR can be calculated by using the 'optically-weighted' BSR $R_w(z)$ instead of $R(z)$ in Eq. (20). $R_w(z_i)$ profiles can be obtained from Eq. (9) by using Eqs. (10)–(11), that is,

$$R_w(z_i) = \frac{R^{att}(z_i)}{\exp[-2 \cdot \tau_c(z_L)]} = \frac{R^{att}(z_i)}{TT^2(z_L)} \quad (21)$$

where $z_L: z_1 < z_i < z_2$. Therefore, $R_w(z_i)$ for the Ci cloud can be determined from Eq. (21), once the "attenuated" backscattering ratio $R^{att}(z_i)$ is calculated from the Eq. (7), and the CCOD $\tau_c(z_L)$ is estimated from Eq. (15).

By using $R_w(z)$ instead of $R(z)$ in Eq (20), the first 'approximate' LR obtained from Eq. (20) is consider as an initial value, which is introduced in a iterative procedure to obtain a more consistent and reliable LR (no linear approach). The final iteration is focused on the no-fluctuation 'stable' tendency of this LR value. Once this final LR is obtained,

this value is regarded as the 'true' *LR* for the Ci cloud layer. Next, this procedure is described in more detail.

A.3. Iterative approach to calculate the 'true' Lidar Ratio (LR) for Ci clouds

The method is based on the following iterative (no linear) approach, as detailed step-by-step next:

1) The first 'a priori' *LR* value calculated in Sect. A2.2 is used as an initial value, which is introduced in Eq. (19) to obtain the initial extinction coefficients $\sigma_c(z)$ for the Ci cloud:

$$\sigma_c(z) = LR \cdot \beta_m(z) \cdot [R_w(z) - 1]. \tag{22}$$

2) Once $\sigma_c(z)$ is calculated (Eq. (22)), an initial set of 'discrete' optical depths $\tau_c(z_i)$are estimated by Eq. (10), where the integral is performed from z_1 up to each height-level z_i within the cloud layer:

$$\tau_c(z_i) = \int_{z_1}^{z_i} \sigma_c(z) \cdot dz. \tag{23}$$

Hence, an optical depth of the Ci layer is obtained when $z_i = z_2$ (top Ci boundary) in Eq. (23), the same $\tau_c(z_L)$ value as that calculated from Eq. (15).

3) A new profile of $R_w(z_i)$ is determined by using Eq. (21), where the CCOD $\tau_c(z_L)$ is replaced by those previously calculated 'discrete' $\tau_c(z_i)$ (Eq. (23)) at each height-level z_i, and $R^{att}(z_i)$ is the profile obtained from Eq. (7).

4) This 'new' profile for $R_w(z)$ is then introduced in Eq. (20), instead of $R(z)$, performing the integral along the overall cloud layer z_L. Hence, a 'new' *LR* value is obtained by using $\tau_c(z_L)$ previously calculated (Eq. (15)).

5) This 'new' *LR* is compared to the initial value. In case the difference between these two LR values is higher than a given convergence factor, this process is iteratively repeated from step 1, but using the 'new' *LR* instead of the previous value. Another 'new' profiles of $\sigma_c(z)$ (step 2) and $R_w(z)$ (step 3) are also generated.

6) Consecutive iterations are performed until that difference is lower than the selected convergence factor (i.e., 10^{-3}). In this case for the Ci cloud layer, the final *LR* value calculated is considered the 'true' LR for the Ci cloud layer, and, likewise, the $R_w(z)$ profile derived in the last iteration is the corresponding BSR profile *R(z)* of the Ci cloud.

A.4. Determination of the height boundaries for both the base and top of the Ci cloud layer

A threshold function *thR*(*z*) is used to determine the higher and lower limits of the Ci cloud layer, z^{top} and z^{base}, respectively. The sharp distinction of the $R^{att}(z)$ with respect to Rayleigh backgrounds in both the cloud boundaries is one of the factors to define this function. The expression of *thR*(*z*) used in this work is a modified version of that used in Larroza et al. (2013), i.e.,

$$thR(z) = 1 + a \cdot R^{att}(z) \tag{24}$$

where $R^{att}(z)$ is the "attenuated" backscattering ratio (Eq. (7)), and *a* is a particular parameter used to obtain a significant cloud detection. The value of *a* is 'experimentally' determined so that z^{top} and z^{base} are found under the condition that the difference between $R^{att}(z)$ and *thR*(*z*) is higher than a given value *b* at both base and top cloud boundaries.

The definition of this threshold function *thR*(*z*) and, in particular, the designation of a given value to the parameter *a* and the difference factor *b*, depend on the lidar system used and the measurement settings applied. In this work, $a = 0.1$ and $b = 0.1$ were applied.

A.5. Multiple scattering effect correction

In the case of Ci clouds, the multiple scattering affects lidar systems, causing an underestimation of the particle extinction, and hence of the CCOD (Wandinger, 1998). In order to obtain the single-scattering CCOD (and LR) values, the measured, multiple-scattering affected (also named 'apparent'), extinction must be corrected by a given factor: the multiple scattering factor, η. The expression of this factor for Ci clouds (Chen et al., 2002) used in this work is adopted from Chen et al. (2002):

$$\eta = \frac{\tau_c(z_L)}{\exp[\tau_c(z_L)] - 1}. \tag{25}$$

Hence, both the retrieved CCOD $\tau_c(z_L)$ and the lidar ratio *LR* values (see Appendix A.2) are corrected by this factor (Eq. (25)) by using the terms (Josset et al., 2012; Garnier et al., 2015; Kienast-Sjögren et al., 2016)

$$\tau_{SS}(z_L) = \frac{\tau_c(z_L)}{\eta} \tag{26}$$

and

$$LR_{SS} = \frac{LR}{\eta} \tag{27}$$

where $\tau_{SS}(z_L)$ and LR_{SS} are, respectively, the 'single-scattering' CCOD and LR values once corrected by multiple scattering effects. For simplicity, the 'SS' subscript is removed in both terms, and they correspond to the corrected CCOD and LR values shown in this work; otherwise, it is indicated.

A.6. Uncertainty analysis

The uncertainty analysis performed in this work is based on error propagation techniques. Hence, the expressions used for calculating the uncertainty of, in particular, the CCOD ($\Delta\tau_c$) and LR (ΔLR), among other variables, are exposed next.

The error corresponding to the CCOD is expressed as

$$\Delta\tau_c = \frac{\Delta TT}{TT}, \tag{28}$$

where ΔTT is the error of the transmittance *TT*, as calculated from the expression:

$$\Delta TT = \frac{1}{2} \cdot TT \cdot \left[\frac{\Delta R^{att}(z<z_1)}{R^{att}(z<z_1)} + \frac{\Delta R^{att}(z>z_2)}{R^{att}(z>z_2)} \right] \tag{29}$$

being, in its turn, $\Delta R^{att}(z<z_1)$ and $\Delta R^{att}(z>z_2)$ the errors associated to R^{att} in the intervals below and above, respectively, the Ci layer (see Sect. A.2, Eqs. (13) and (14)). The error for R^{att} is expressed as

$$\Delta R^{att} = R^{att} \cdot \left[\frac{\Delta P_r}{P_r} + \frac{\Delta C}{C} \right], \tag{30}$$

where ΔP_r and ΔC are the errors corresponding, respectively, to the lidar RCS P_r and the calibration constant *C*. All other terms are defined before.

Regarding the error for the LR, it can be expressed as

$$\Delta LR = LR \cdot \left[\frac{\Delta\tau_c}{\tau_c} + \frac{\Delta B}{B} \right], \tag{31}$$

where $\Delta\tau_c$ is calculated from Eq. (28), and $B = \int_{z_1}^{z_2} \beta_m(z) \cdot [R(z) - 1] \cdot dz$ (see Sect. A.2, Eq. (20)); the error ΔB can be calculated from the

expression:

$$\Delta B = \int_{z_1}^{z_2} \beta_m(z) \cdot \Delta R(z) \cdot dz, \tag{32}$$

being the error for R estimated as

$$\Delta R = R \cdot \left[\frac{\Delta R^{att}}{R^{att}} + 2 \cdot \frac{\Delta TT}{TT} \right]. \tag{33}$$

The errors ΔTT and ΔR^{att} are obtained from Eqs. (29) and (30), respectively.

Finally, the errors associated to the single-scattering CCOD (τ_{SS}) and LR (LR_{SS}) from Eqs. (26) and (27), respectively, are calculated from the expressions:

$$\Delta\tau_{SS} = \tau_{SS} \cdot \left[\frac{\Delta\tau_c}{\tau_c} + \frac{\Delta\eta}{\eta} \right] \tag{34}$$

and

$$\Delta LR_{SS} = LR_{SS} \cdot \left[\frac{\Delta LR}{LR} + \frac{\Delta\eta}{\eta} \right], \tag{35}$$

where $\Delta\eta$ can be expressed as

$$\Delta\eta = \eta \cdot \left[\frac{\Delta\tau_c}{\tau_c} + \frac{\Delta\tau_c \cdot \exp[\tau_c]}{\exp[\tau_c] - 1} \right]. \tag{36}$$

References

Barbosa, H.M.J., Barja, B., Pauliquevis, T., Gouveia, D.A., Artaxo, P., Cirino, G.G., Santos, R.M.N., Oliveira, A.B., 2014. A permanent Raman lidar station in the Amazon: description, characterization, and first results. Atmos. Meas. Tech. 7, 1745–1762. http://dx.doi.org/10.5194/amt-7-1745-2014.

Baum, B.A., Yang, P., Heymsfield, A.J., Schmitt, C., Xie, Y., Bansemer, A., Hu, Y.X., Zhang, Z., 2011. Improvements to shortwave bulk scattering and absorption models for the remote sensing of ice clouds. J. Appl. Meteor. Clim. 50, 1037–1056. http://dx.doi.org/10.1175/2010JAMC2608.1.

Boucher, O., 1999. Air traffic may increase cirrus cloudiness. Nature 397, 30–31.

Boucher, O., Randall, D., Artaxo, P., Bretherton, C., Feingold, G., Forster, P., Kerminen, V.-M., Kondo, Y., Liao, H., Lohmann, U., Rasch, P., Satheesh, S.K., Sherwood, S., Stevens, B., Zhang, X.Y., 2013. Clouds and aerosols. In: Stocker, T.F., Qin, D., Plattner, G.-K., Tignor, M., Allen, S.K., Boschung, J., Nauels, A., Xia, Y., Bex, V., Midgley, P.M. (Eds.), Climate Change 2013: The Physical Science Basis. Contribution of Working Group I to the Fifth Assessment Report of the Intergovernmental Panel on Climate Change. Cambridge University Press, Cambridge, United Kingdom and New York, NY, USA.

Burkhardt, U., Kärcher, B., 2011. Global radiative forcing from contrail cirrus. Nat. Clim. Chang. 1, 54–58.

Campbell, J.R., Hlavka, D.L., Welton, E.J., Flynn, C.J., Turner, D.D., Spinhirne, J.D., Scout, V.S., Hwang, I.H., 2002. Full-time, eye-safe cloud and aerosol Lidar observation at Atmospheric Radiation Measurement program sites: instrument and data processing. J. Atmos. Oceanic Technol. 19, 431–442.

Campbell, J.R., Vaughan, M.A., Oo, M., Holz, R.E., Lewis, J.R., Welton, E.J., 2015. Distinguishing cirrus cloud presence in autonomous lidar measurements. Atmos. Meas. Tech. 8, 435–449. http://dx.doi.org/10.5194/amt-8-435-2015.

Campbell, J.R., Lolli, S., Lewis, J.R., Gu, Y., Welton, E.J., 2016. Daytime cirrus cloud top-of-the-atmosphere radiative forcing properties at a midlatitude site and their global consequences. J. Appl. Meteor. Climatol. 55 (8), 1667–1679. http://dx.doi.org/10.1175/JAMC-D-15-0217.1.

Chen, W.N., Chiang, C.W., Nee, J.B., 2002. Lidar ratio and depolarization ratio for cirrus clouds. Appl. Optics 41, 6470–6476. http://dx.doi.org/10.1364/AO.41.006470.

Córdoba-Jabonero, C., Gil, M., Yela, M., Maturilli, M., Neuber, R., 2009. Polar stratospheric cloud observations in the 2006/07 arctic winter by using an improved micro pulse Lidar. J. Atmos. Ocean. Technol. 26, 2136–2148.

Córdoba-Jabonero, C., Guerrero-Rascado, J.L., Toledo, D., Parrondo, M., Yela, M., Gil, M., Ochoa, H.A., 2013. Depolarization ratio of polar stratospheric clouds in coastal Antarctica: comparison analysis between ground-based micro pulse Lidar and space-borne CALIOP observations. Atmos. Meas. Tech. 6, 703–717.

Das, S.K., Chiang, C.W., Nee, J.B., 2009. Characteristics of cirrus clouds and its radiative properties based on lidar observation over Chung-Li, Taiwan. Atmos. Res. 93, 723–735.

Dupont, J.-C., Haeffelin, M., 2008. Observed instantaneous cirrus radiative effect on surface-level shortwave and longwave irradiances. J. Geophys. Res. 113, D21202. http://dx.doi.org/10.1029/2008JD009838.

Dupont, J.-C., Haeffelin, M., Morille, Y., Noël, V., Keckhut, P., Winker, D., Comstock, J., Chervet, P., Roblin, A., 2010. Macrophysical and optical properties of midlatitude cirrus clouds from four ground-based lidars and collocated CALIOP observations. J. Geophys. Res. 115, D00H24. http://dx.doi.org/10.1029/2009JD011943.

Garnier, A., Pelon, J., Vaughan, M.A., Winker, D.M., Trepte, C.R., Dubuisson, P., 2015. Lidar multiple scattering factors inferred from CALIPSO lidar and IIR retrievals of semi-transparent cirrus cloud optical depths over oceans. Atmos. Meas. Tech. 8, 2759–2774. http://dx.doi.org/10.5194/amt-8-2759-2015.

Giannakaki, E., Balis, D.S., Amiridis, V., Kazadzis, S., 2007. Optical and geometrical characteristics of cirrus clouds over a southern European lidar station. Atmos. Chem. Phys. 7, 5519–5530.

Guerrero-Rascado, J.L., Landulfo, E., Antuña, J.C., Barbosa, H.M.J., Barja, B., Bastidas, A.E., Bedoya, A.E., da Costa, R.F., Estevan, R., Forno, R.N., Gouveia, D.A., Jimenez, C., Larroza, E.G., Lopes, F.J.S., Montilla-Rosero, E., Moreira, G.A., Nakaema, W.M., Nisperuza, D., Alegria, D., Múnera, M., Otero, L., Papandrea, S., Pawelko, E., Quel, E.J., Ristori, P., Rodrigues, P.F., Salvador, J., Sánchez, M.F., Silva, A., 2016. Latin American Lidar Network (LALINET) for aerosol research: diagnosis on network instrumentation. J Atmos. Sol. Terr. Phys. 138–139, 112–120.

Guo, J., Liu, H., Wang, F., Huang, J., Xia, F., Lou, M., Wu, Y., Jiang, J.H., Xie, T., Zhaxi, Y., Yung, Y.L., 2016. Three-dimensional structure of aerosol in China: a perspective from multi-satellite observations. Atmos. Res. 178-179, 580–589. http://dx.doi.org/10.1016/j.atmosres.2016.05.010.

He, Q.S., Li, C.C., Ma, J.Z., Wang, H.Q., Shi, G.M., Liang, Z.R., Luan, Q., Geng, F.H., Zhou, X.W., 2013. The properties and formation of cirrus clouds over the Tibetan plateau based on summertime Lidar measurements. J. Atmos. Sci. 70, 901–915.

Hostetler, C.A., Liu, Z., Reagan, J., Vaughan, M.A., Winker, D.M., Osborn, M., Hunt, W.H., Powell, K.A., Trepte, C., 2006. CALIOP Algorithm Theoretical Basis Document – Calibration and level 1 Data Products. Release 1.0, PC-SCI-201 Part 1. NASA Langley Research Center, Hampton, Virginia, USA (available at: http://www-calipso.larc.nasa.gov/resources/project_documentation.php (last access: 06 November 2014)).

Hu, Y., Winker, D., Vaughan, M., Lin, B., Omar, A., Trepte, C., Flittner, D., Yang, P., Nasiri, S.L., Baum, B., Holz, R., Sun, W., Liu, Z., Wang, Z., Young, S., Stamnes, K., Huang, J., Kuehn, R., 2009. CALIPSO/CALIOP cloud phase discrimination algorithm. J. Atmos. Ocean. Tech. 26, 2293–2309. http://dx.doi.org/10.1175/2009JTECHA1280.1.

Iacono, M.J., Delamere, J.S., Mlawer, E.J., Shephard, M.W., Clough, S.A., Collins, W.D., 2008. Radiative forcing by long-lived greenhouse gases: calculations with the AER radiative transfer models. J. Geophys. Res. Atmos. 113, D13103.

Iwasaki, S., Luo, Z.J., Kubota, H., Shibata, T., Okamoto, H., Ishimoto, H., 2015. Characteristics of cirrus clouds in the tropical lower stratosphere. Atmos. Res. 164–165, 358–368. http://dx.doi.org/10.1016/j.atmosres.2015.06.009.

Josset, D., Pelon, J., Garnier, A., Hu, Y., Vaughan, M., Zhai, P.W., Kuehn, R., Lucker, P., 2012. Cirrus optical depth and lidar ratio retrieval from combined CALIPSO-CloudSat observations using ocean surface echo. J. Geophys. Res. 117 (D5), D05207.

Kienast-Sjögren, E., Rolf, C., Seifert, P., Krieger, U.K., Luo, B.P., Krämer, M., Peter, T., 2016. Radiative properties of mid-latitude cirrus clouds derived by automatic evaluation of lidar measurements. Atmos. Chem. Phys. 16, 7605–7621. http://dx.doi.org/10.5194/acp-16-7605-2016.

Kim, Y., Kim, S., Kim, M., Yoon, S., 2014. Geometric and optical properties of cirrus clouds inferred from three-year ground-based lidar and CALIOP measurements over Seoul, Korea. Atmos. Res. 139, 27–35. http://dx.doi.org/10.1016/j.atmosres.2013.12.016.

Krämer, M., Rolf, C., Luebke, A., Afchine, A., Spelten, N., Costa, A., Meyer, J., Zöger, M., Smith, J., Herman, R.L., Buchholz, B., Ebert, V., Baumgardner, D., Borrmann, S., Klingebiel, M., Avallone, L., 2016. A microphysics guide to cirrus clouds – part 1: cirrus types. Atmos. Chem. Phys. 16, 3463–3483. http://dx.doi.org/10.5194/acp-16-3463-2016.

Lakkis, S.G., Lavorato, M., Canziani, P.O., 2009. Monitoring cirrus clouds with lidar in the southern hemisphere: a local study over Buenos Aires. 1. Tropopause heights. Atmos. Res. 92, 18–26.

Larroza, E.G., Nakaema, W.M., Bourayou, R., Hoareau, C., Landulfo, E., Keckhut, P., 2013. Towards an automatic lidar cirrus cloud retrieval for climate studies. Atmos. Meas. Tech. 6, 3197–3210.

Liou, K.-N., 1986. Influence of cirrus clouds on weather and climate processes: a global perspective. Mon. Weather Rev. 114, 1167–1200.

Liu, Z., Vaughan, M., Winker, D., Kittaka, C., Getzewich, B., Kuehn, R., Omar, A., Powell, K., Trepte, C., Hostetler, C., 2009. The CALIPSO lidar cloud and aerosol discrimination: version 2 algorithm and initial assessment of performance. J. Atmos. Ocean. Technol. 26, 1198–1213. http://dx.doi.org/10.1175/2009JTECHA1229.1.

Myhre, G., Shindell, D., Bréon, F.-M., Collins, W., Fuglestvedt, J., Huang, J., Koch, D., Lamarque, J.-F., Lee, D., Mendoza, B., Nakajima, T., Robock, A., Stephens, G., Takemura, T., Zhang, H., 2013. Anthropogenic and natural radiative forcing. In: Stocker, T.F., Qin, D., Plattner, G.-K., Tignor, M., Allen, S.K., Boschung, J., Nauels, A., Xia, Y., Bex, V., Midgley, P.M. (Eds.), Climate Change 2013: The Physical Science Basis. Contribution of Working Group I to the Fifth Assessment Report of the Intergovernmental Panel on Climate Change. Cambridge University Press, Cambridge, United Kingdom and New York, NY, USA.

Platt, C.M.R., 1973. Lidar and radiometric observations of cirrus clouds. J. Atmos. Sci. 30, 1191–1204. http://dx.doi.org/10.1175/1520-0469(1973)030<1191:LAROOC>2.0.CO;2.

Platt, C.M.R., Dilley, A.C., 1981. Remote sounding of high clouds. IV: Observed temperature variations in cirrus optical properties. J. Atmos. Sci. 38, 1069–1082.

Platt, C.M.R., Scott, J.C., Dilley, A.C., 1987. Remote sounding of high clouds VI: optical properties of mid latitude and tropical cirrus. J. Atmos. Sci. 44, 729–747.

Platt, C.M.R., Young, S.A., Austin, R.T., Patterson, G.R., Mitchell, D.L., Miller, S.D., 2002. LIRAD observations of tropical cirrus clouds in MCTEX. Part I: optical properties and detection of small particles in cold cirrus. J. Atmos. Sci. 59, 3145–3162. http://dx.doi.org/10.1175/1520-0469(2002)059<3145:LOOTCC>2.0.CO;2.

Sassen, K., Campbell, J.R., 2001. A midlatitude cirrus cloud climatology from the Facility for Atmospheric Remote Sensing. Part I: macrophysical and synoptic properties. J. Atmos. Sci. 58, 481–496.

Sassen, K., Cho, B.S., 1992. Subvisual-thin cirrus lidar dataset for satellite verification and climatological research. J. Appl. Meteor. 31, 1275–1285. http://dx.doi.org/10.1175/1520-0450(1992)031<1275:STCLDF>2.0.CO;2.

Sassen, K., Comstock, J., 2001. A midlatitude cirrus cloud climatology from the facility for atmospheric remote sensing. Part III: radiative properties. J. Atmos. Sci. 58 (5), 2113–2127.

Sassen, K., Grin, M., Dood, G.C., 1989. Optical scattering and microphysical properties of subvisual cirrus clouds and climatic implications. J. Appl. Meteor. 28, 91–98.

Sassen, K., Wang, Z., Liu, D., 2008. Global distribution of cirrus clouds from CloudSat/cloud-aerosol lidar and Infrared pathfinder satellite observations (CALIPSO) measurements. J. Geophys. Res. 113, D00A12. http://dx.doi.org/10.1029/2008JD009972.

Seifert, P., Ansmann, A., Müller, D., Wandinger, U., Althausen, D., Heymsfield, A.J., Massie, S.T., Schmitt, C., 2007. Cirrus optical properties observed with lidar, radiosonde, and satellite over the tropical Indian Ocean during the aerosol-polluted northeast and clean maritime southwest monsoon. J. Geophys. Res. 112, D17205. http://dx.doi.org/10.1029/2006JD008352.

Stephens, G.L., 2005. Cloud feedbacks in the climate system: a critical review. J. Clim. 18, 237–273.

Thorsen, T., Fu, Q., 2015. Automated retrieval of cloud and aerosol properties from the ARM Raman lidar. Part II: extinction. J. Atmos. Oceanic Technol. 32, 1999–2023. http://dx.doi.org/10.1175/JTECH-D-14-00178.1.

Vaughan, M.A., Powell, K.A., Kuehn, R.E., Young, S.A., Winker, D.M., Hostetler, C.A., Hunt, W.H., Liu, Z., McGill, M.J., Getzewich, B.J., 2009. Fully automated detection of cloud and aerosol layers in the CALIPSO Lidar measurements. J. Atmos. Oceanic Tech. 26, 2034–2050. http://dx.doi.org/10.1175/2009JTECHA1228.1.

Vaughan, M.A., Liu, Z., McGill, M.J., Hu, Y., Obland, M.D., 2010. On the spectral dependence of backscatter from cirrus clouds: assessing CALIOP's 1064 nm calibration assumptions using cloud physics lidar measurements. J. Geophys. Res. 115, D14206. http://dx.doi.org/10.1029/2009JD013086.

Wandinger, U., 1998. Multiple-scattering influence on extinction- and backscatter-coefficient measurements with Raman and high-spectral resolution lidars. Appl. Opt. 37, 417–427.

Welton, E.J., Campbell, J.R., Spinhirne, J.D., Scott, V.S., 2001. Global monitoring of clouds and aerosols using a network of micro-pulse lidar systems. In: Singh, U.N., Itabe, T., Sugimoto, N. (Eds.), Lidar Remote Sensing for Industry and Environmental Monitoring. Proc. SPIE 4153, pp. 151–158.

Winker, D.M., Vaughan, M.A., Omar, A., Hu, Y., Powell, K.A., Liu, Z., Hunt, W.H., Young, S.A., 2009. Overview of the CALIPSO mission and CALIOP data processing algorithms. J. Atmos. Ocean. Technol. 26, 2310–2323. http://dx.doi.org/10.1175/2009JTECHA1281.1.

Yang, H.Y., Dobbie, S., Herbert, R., Connolly, P., Gallagher, M., Ghosh, S., Al-Jumur, S.M.R.K., Clayton, J., 2012. The effect of observed vertical structure, habits, and size distributions on the solar radiative properties and cloud evolution of cirrus clouds. Q. J. R. Meteorol. Soc. 138, 1221–1232. http://dx.doi.org/10.1002/qj.973.

Yorks, J.E., McGill, M., Rodier, S., Vaughan, M., Hu, Y., Hlavka, D., 2009. Radiative effects of African dust and smoke observed from clouds and the earth's radiant energy system (CERES) and cloud-aerosol lidar with orthogonal polarization (CALIOP) data. J. Geophys. Res. 114, D00H04. http://dx.doi.org/10.1029/2009JD012000.

Yorks, J.E., Hlavka, D.L., Vaughan, M.A., McGill, M.J., Hart, W.D., Rodier, S., Kuehn, R., 2011. Airborne validation of cirrus cloud properties derived from CALIPSO lidar measurements: spatial properties. J. Geophys. Res. 116, D19207. http://dx.doi.org/10.1029/2011JD015942.

Young, S.A., 1995. Analysis of lidar backscatter profiles in optically thin clouds, Appl. Optics 34, 7019–7031. http://dx.doi.org/10.1364/AO.34.007019.

Young, S.A., Vaughan, M.A., 2009. The retrieval of profiles of particulate extinction from cloud aerosol Lidar infrared pathfinder satellite observations (CALIPSO) data: algorithm description. J. Atmos. Ocean. Technol. 26, 1105–1119. http://dx.doi.org/10.1175/2008 JTECHA1221.1.

Zhang, D., Luo, T., Liu, D., Wang, Z., 2014. Spatial scales of altocumulus clouds observed with collocated CALIPSO and CloudSat measurements. Atmos. Res. 149, 58–69. http://dx.doi.org/10.1016/j.atmosres.2014.05.023.